Research Square

Preprints are preliminary reports that have not undergone peer review.
They should not be considered conclusive, used to inform clinical practice,
or referenced by the media as validated information.

Mechanistic insights into Mtb effector EspB-mediated mitochondrial membrane damage

Somnath Dutta

somnath@iisc.ac.in

Indian Institute of Science https://orcid.org/0000-0002-3181-0108

Dipanwita Mandal

Indian Institute of Science

Aishita Chakraborty

Indian Institute of Science

Arnab Chatterjee

Indian Institute of Science

Patrick D'Silva

Indian Institute of Science

Article

Keywords: EspB, Tom70, cryo-EM, Mtb, Mitochondria, NS-TEM, MST

Posted Date: November 4th, 2026

DOI: https://doi.org/10.21203/rs.3.rs-11278229/v1

License: This work is licensed under a Creative Commons Attribution 4.0 International License.
Read Full License

Additional Declarations: There is no duality of interest

Abstract

Mycobacterium tuberculosis (*Mtb*) utilises the ESX-1 type VII secretion system to export effector proteins, such as EspB, which ablate phagosome maturation, damage mitochondria, and lead to host-cell death. EspB assembles a heptameric oligomer under acidic and lipid-rich conditions. It interacts with mitochondrial lipids, mainly phosphatidic acid (PA), phosphatidylethanolamine (PE), and phosphatidylserine (PS) via its C-terminal region. However, the precise molecular mechanism remains unknown. Our current study demonstrates that EspB targets host mitochondria by coordinating interactions with both mitochondrial lipid and outer membrane protein Tom70. Biophysical, biochemical, and single-particle cryo-EM analyses revealed the structural architecture of the EspB-Tom70 complex, identifying key residues at the interaction interface. A mutagenesis study reveals that disruption of EspB-Tom70 complex formation reduces cellular cytotoxicity and mitochondrial damage in cellular assays, establishing a functional role for this interaction during infection. Together, these findings elucidate how *Mtb* hijacks host mitochondrial machinery through EspB to drive host-cell death during infection.

Introduction

Tuberculosis, caused by *Mycobacterium Tuberculosis (Mtb)*, remains one of the leading causes of death from infectious diseases worldwide, accounting for over 1.25 million deaths in 2023[1], reflecting the pathogen's ability to establish a persistent intracellular niche within host macrophages [2,3]. *Mtb* is distinguished by its complex, lipid-rich cell envelope, which includes a mycomembrane composed of peptidoglycan, arabinogalactan, and long-chain mycolic acids[4–8]. This highly impermeable, hydrophobic barrier limits antibiotic penetration and necessitates a specialised secretion system to export virulence factors that modulate host cell processes[2,5,8]. Among these, the type VII secretion systems (T7SS), encoded by five paralogous ESX loci (ESX-1 to ESX-5), play the central role in *Mtb* pathogenesis [9–13]. In particular, the ESX-1 plays a crucial role in virulence and is required for phagosomal escape, host immune modulation and intracellular survival [10,12,14–18]. A set of genes present in the ESX-1 locus (RD1) is deleted in the attenuated Bacillus Calmette Guérin (BCG) vaccine, highlighting their essential role in virulence [19,20]. The ESX-1 apparatus consists of core membrane components, including EccC, EccD, and EccB [19,21,22], as well as the protease MycP1 [23,24] and a set of secreted substrates, such as EspB, ESAT-6, CFP10, and EspC [7,10,19,25–27]. While the roles of ESAT-6 and CFP-10 in membrane disruption and host immune modulation have been widely studied, the functional contributions of proteins encoded within the extended RD1 region remain less well defined [15,20,28,29]. Emerging evidence suggests that these extended regions play a significant role in fine-tuning host-pathogen interactions beyond phagosomal escape[27]. EspB, encoded within this extended RD1 region, has emerged as a critical effector of *Mtb* pathogenicity [27].

Genetic and functional studies have demonstrated that disruption of EspB results in a significant reduction in haemolytic activity and cytotoxicity, impairs phagosomal maturation, and ultimately enhances host survival in infection models [27,30–33]. EspB is synthesised as a 50 kDa precursor and

undergoes proteolytic processing by the ESX-1-associated protease MycP1, which is essential for its secretion and activity [27,34]. Following secretion, EspB localises to the host cytosol, where it is proposed to associate with the host membrane and assemble into oligomers [35,36]. Previous studies have shown that it oligomerises upon binding to specific phospholipids [32,] which are enriched in both the phagosome and the mitochondrial outer membrane [37,38]. Importantly, PA plays a role in mitochondrial dynamics by regulating fusion and fission, and it also functions as an apoptotic marker [38]. Mitochondria play an important role in innate immunity, serving as a hub for metabolic signalling, reactive oxygen species production, and regulation of apoptosis [39–41]. In previous studies, EspB has been observed to cluster and localise at the site of mitochondrial membrane damage [42]. However, an *in vitro* leakage assay using a model membrane mimicking the lipid composition of the outer mitochondrial membrane (OMM) has failed to demonstrate membrane permeabilisation by EspB alone, suggesting that additional host factors, such as receptor proteins, may be required to mediate its activity [42]. Previously, several other studies, such as ESAT-6-CFP10 interacting with the TLR-2 receptor in macrophages [43], *Helicobacter pylori* interacting with integrin α5β1 [59], and *Vibrio cholerae* binding to the GM1 receptor in epithelial cells [62], have shown similar binding affinity of bacterial effector proteins from various bacterial secretion systems towards host cell receptors for their survival and pathogenesis. Similarly, EspB may interact with the mitochondrial receptor in a similar fashion to contribute to its pathogenesis.

Here, we show that EspB targets and disrupts host mitochondria by associating with both lipid and receptor proteins on the outer mitochondrial membrane (OMM) by using various biochemical assays. We demonstrate that EspB association with mitochondria depends on both lipid and import receptor protein Tom70. Structural studies using Cryo-electron microscopy (Cryo-EM) and Negative Staining Transmission Electron microscopy (NS-TEM) analysis reveal an additional density consistent with Tom70, and interacting-interface analysis identified EspB residues responsible for their association. Mutational studies showed the necessity of these residues in EspB-Tom70 complex formation. Thus, the EspB-Tom70 interactions perturb the mitochondrial membrane and alter mitochondrial physiology, including changes in ATP production and membrane potential, as well as the induction of apoptosis-like cell death in yeast. Together, our findings provide mechanistic insight into how ESX-1-secreted effector proteins, EspB functions extend from phagosomal modulation to targeting host cell organelles and establish an understanding of how *Mycobacterium* pathogens exploit host trafficking pathways to achieve subcellular specificity.

Results

EspB targets mitochondria through coordinated lipid and receptor-mediated interactions.

Previous studies have demonstrated that the active C-terminal region of $EspB_{278–332}$ exhibits a strong affinity for the mitochondrial membranes [44]. Beyond membrane association, the intrinsically disordered C-terminal tail may also mediate interactions with mitochondrial receptor proteins. To elucidate the mechanism underlying EspB association with the mitochondrial outer membrane receptors, a construct

corresponding to the mature EspB (Supplementary Figure **S1A**) was used for all subsequent analyses. EspB was purified using Ni-NTA affinity purification, followed by size-exclusion chromatography, where the peak at 11.48 ml corresponds to the heptameric species (Supplementary Figure **S1B**). SDS-PAGE analysis of this fraction revealed a single band (Supplementary Figure **S1C**), which was further confirmed by Orbitrap mass spectrometry (Supplementary Figure **S1E**). Purified $EspB_{1-332}$ was selected for evaluation of the mitochondrial binding. Therefore, a mitochondrial sedimentation assay was performed with isolated mitochondria and purified EspB-His at multiple time points. EspB was detected predominantly in the supernatant as well as visible in the pellet fractions (Fig. 1A). To confirm the identity of these pellet-associated bands, immunoblotting with an anti-His antibody was performed, which verified the presence of EspB in all pellet fractions (Fig. 1B and Supplementary Figure **S1F**), suggesting association with mitochondria. However, based on these results, we were unable to determine whether EspB associates with the mitochondrial membrane, mitochondrial receptors, or both. To visualise these interactions, room temperature Transmission Electron Microscopy (TEM) was performed. Isolated, untreated mitochondria displayed an intact, continuous bilayer (Supplementary Figure **S1D**). In contrast, incubation with EspB resulted in surface decoration and accumulation of the protein at the site of mitochondrial leakage (Fig. 1C), consistent with previous reports[42].

Further, we performed cryo-EM to investigate the interaction of EspB with the mitochondrial outer membrane, revealing a similar pattern of EspB association with the mitochondrial membrane (Supplementary Fig. 2A). To visualise the overall architecture of the EspB complex, reference-free 2D class averages were calculated, revealing distinct top views of EspB with additional density covering its central pore (Supplementary Figure **S2B**). This density may correspond to the mitochondrial membrane lipids, receptor proteins, or both. To determine whether lipids or protein receptors mediate EspB binding, mitochondria were subjected to proteolytic treatment using Proteinase K, which cleaves all amino acids by hydrolysing peptide bonds of the membrane proteins associated with the outer mitochondrial membrane (OMM). Similarly, Trypsin cleaves lysine and arginine residues in the exposed region of membrane proteins associated with the outer mitochondrial membrane (OMM), leaving the inner mitochondrial membrane (IMM) protein largely intact. Proteinase K- and trypsin-treated mitochondria were incubated with EspB to assess its binding affinity and interaction with mitochondria. Negative-stain TEM and cryo-EM analysis revealed a reduction in EspB association with protease-treated mitochondria due to the loss of proteinaceous membrane receptors (Fig. 1D, 1E, Supplementary Figure **S2A**). Interestingly, protein accumulation at the leakage site was not visible in the NS-TEM micrograph (Fig. 1D, 1E). Quantitative analysis of EspB association with mitochondria from reference-free 2D class averages indicated an approximately 20% decrease in EspB binding in Trypsin- and proteinase K-treated mitochondria compared with the untreated control (Fig. 1F, 1G), suggesting a probable receptor involved in binding.

To confirm the role of mitochondrial receptors, a co-sedimentation assay was performed with EspB and mitochondria, followed by immunoblotting, which showed a substantial reduction in EspB in the pellet fraction after trypsin treatment and a near-complete loss after proteinase K treatment (Supplementary

Figure **S1G**). These results are consistent with our TEM data, indicating that mitochondrial receptors most likely play a significant role in mediating EspB-mitochondria interactions. Consistent with this observation, a small fraction of EspB remained associated with mitochondria even after proteinase K and trypsin treatment, suggesting low-affinity, lipid-mediated interactions of EspB as reported earlier [32,42]. However, given the low abundance of lipids such as phosphatidic acid and phosphatidylserine in the outer mitochondrial membrane, lipids alone are insufficient to account for the observed binding. Collectively, these findings suggest that EspB associates with the mitochondrial membrane via both lipid and outer-membrane receptor proteins. However, further validation is required to establish the receptor-mediated interaction of EspB. It is also important to identify the specific protein receptor(s) responsible for EspB interaction.

EspB interacts with mitochondrial receptor protein Tom70.

To identify mitochondrial receptor proteins, a co-immunoprecipitation assay was performed after treating isolated mitochondria with digitonin, a mild, non-ionic detergent that selectively permeabilises the OMM. This assay yielded multiple discrete bands in addition to the EspB band on SDS-PAGE (Fig. 1H), suggesting the presence of interacting partners at the mitochondrial surface. These bands were excised, digested with Trypsin, and analysed by mass spectrometry using an Orbitrap. The resulting spectra indicated that Tom70 and porin were receptor proteins with EspB. Therefore, Tom70 and porin were potentially involved in EspB binding, along with an outer mitochondrial membrane (OMM) lipid (Fig. 2A, **Table 1**). Representative spectra with the highest Xcorr and lowest q values were shown (Supplementary Figure **S2C**, **S2D**), providing high confidence in the predicted results.

To understand the specificity of the interaction, a co-immunoprecipitation assay was performed using anti-Tom70 and anti-porin antibodies. EspB showed a strong interaction with Tom70 and a transient interaction with porin (Fig. 2B). Our findings further indicate that EspB interacts with Tom70. These results are consistent with our earlier observations and collectively suggest that Tom70 functions as a receptor for EspB.

Also, previous studies have established that Tom70, a receptor located on the outer mitochondrial membrane, plays a crucial role in the import of precursor proteins into mitochondria [45,46]. Therefore, it is possible that EspB follows a similar pathway and interacts with mitochondria through the mitochondrial Tom70 receptor protein.

To validate our hypothesis, purified Tom70 and EspB proteins should be directly used to determine the binding affinity between them. Thus, Tom70 was cloned and purified using Ni-NTA followed by SEC. The SEC revealed a peak at around 12.3 ml (blue dotted line), corresponding to the dimeric form (Supplementary Figure **S3A**). The purity and identity of the protein were confirmed by SDS PAGE and MALDI-TOF mass spectrometry (Supplementary Figure **S3B** and **S3C**). We first quantified the binding affinity between purified EspB and Tom70 using microscale thermophoresis (MST), which yields a binding affinity in the nanomolar range (K_d of 131.5 nM) (Fig. 2C). To investigate the EspB-Tom70

complex formation, EspB (heptamer) and Tom70 (dimer) complexes were incubated at a 1:2 ratio and analysed by SEC, where three distinct peaks were observed. Two peaks corresponding to individual protein peaks: EspB at 11.48 mL (350 kDa, marked in red) and Tom70 at 12.8 mL (150 kDa, marked in blue) (Fig. 2D). Remarkably, an additional peak was observed at 9.7mL (green) and was further confirmed by SDS-PAGE, where two bands at 75-kDa (Tom70) and 50-kDa (EspB) were observed (Fig. 2D and Supplementary Figure **S3E**). To identify overall structural insight into the EspB-Tom70 complex, transmission electron microscopy of the complex peak was performed, which showed an elongated particle likely representing an assembled EspB-Tom70 complex (Supplementary Figure S**3D**). In contrast, the remaining two peaks predominantly consist of individual EspB and Tom70 species (Supplementary Figure **S3D**). Reference-free 2D class averages from the cryo-EM studies revealed canonical top and side views of EspB, with additional density at the bottom, consistent with our previous findings [42] (Fig. 3E). Together, these findings indicate that EspB binds to mitochondria through interaction with the outer membrane receptor protein Tom70.

Structural analysis reveals the formation of the EspB complex with Tom70.

To differentiate the structural changes of EspB in receptor-bound form, we performed the high-resolution structural analysis of control EspB using Cryo-EM. Cryo-EM micrographs of EspB showed a circular ring-like top view and parallel lines in side views (Supplementary Figure **S4**), consistent with oligomeric assemblies [42]. Reference-free 2D classification yielded well-defined class averages displaying a ring-like structure indicative of heptameric assembly (Supplementary Figure **S4**). The 3D-reconstructed cryo-EM density map of EspB with a global resolution of 3.2 Å showed a similar heptameric assembly coloured differently (**PDB-26UN**), in agreement with previous reports (Fig. 3A)[42,44,47,48]. The overall local resolution ranged from 3.2 to 3.8 Å (Supplementary Figure **S5A**). Side-chain fitting of the EspB model in the cryo-EM map indicated the overall quality of the map (Fig. 3B, Supplementary Figure **S5C**). Structural comparison with the previously reported structure (**PDB-6XZC**) revealed some structural shifts at different positions. Notably, residue P289 in the C-terminal region is displaced by 12.59 Å, while residues T8, E127, and S251 exhibit negligible shifts of 2.1, 4.47, and 2.08 Å, respectively (Fig. 3C and Supplementary Figure **S5B**). Importantly, our map also revealed an additional density that was not accounted for in the previous model (**PDB-6XZC**). This density was unambiguously assigned to residues G125 and E126 following atomic model building [81] (Fig. 3D), which had not been confidently resolved in the previous model (**PDB-6XZC)**. This cryo-EM study of EspB would provide a foundation for structural characterisation of the EspB–Tom70 complex.

To structurally characterise the basis of the EspB–Tom70 interaction, single-particle cryo-EM was used, and the following data processing pipeline was followed as mentioned in (Supplementary Figure **S6**). Raw micrographs revealed an additional density at the bottom of EspB (marked in red) compared with EspB alone (Fig. 3E). Similarly, a reference-free 2D class average displayed an additional density that blocked the central pore in top views, along with a protrusion near the C-termini in the side view (Fig. 2E). Due to the intrinsic symmetry mismatch between heptameric EspB and dimeric Tom70, 3D reconstruction was performed without symmetry constraints (C1) to capture potential conformational

variability. The resulting 3D refined cryo-EM map of EspB-Tom70 was obtained at 5.08 Å (**EMDB:81473**) (Fig. 3E). The EspB heptamer was well resolved, with individual protomers coloured separately, and an additional density was observed at the bottom of EspB (marked in red), proximal to the C-terminal of EspB, corresponding to Tom70 density (Fig. 3E**)**. For better visualisation, a cross-sectional view of the complex is shown, revealing the spatial arrangement of all EspB protomers (blue) along with the peripheral density assigned to Tom70 (grey) (Supplementary Figure **S7D**).

Despite a strong density of Tom70 in the map, it remained poorly resolved compared to EspB. The local resolution of EspB ranges from 4.5 to 6 Å, whereas the resolution of Tom70 is 10 Å (Supplementary Figure **S7C**). To investigate the weakly resolved Tom70 density of EspB-Tom70 complex, 3D hetero-refinement was performed, which revealed substantial positional heterogeneity of Tom70 relative to EspB protomers (marked in red) (Fig. 3F). 3D hetero-refinement separated the particles into three different conformational states (State 1: **EMDB-81473**, State 2: EMDB-**81461**, and State 3: EMDB-**81462**), where Tom70 adopted distinct conformations, protruding either outward or inward relative to the EspB assembly across different 2D classes (yellow arrows), indicating substantial conformational heterogeneity within the complex (Supplementary Figure S8A). Together, these findings suggest that symmetry mismatch, conformational heterogeneity, and Tom70 flexibility reduce effective particle averaging during reconstruction and limit the resolution of EspB-Tom70 interaction. Nevertheless, our Cryo-EM-based structural analyses provide evidence consistent with our biochemical and biophysical findings, collectively supporting a strong interaction between EspB and Tom70.

EspB and Tom70 structural interaction

To define the interactions between EspB and Tom70, we performed rigid-body docking using the EspB atomic model generated in this study (**PDB: 26UN**) and the reported crystal structure of Tom70 (**PDB: 2GW1**) [49]. Although during our structure refinement, we were unable to obtain the full 3D structure of Tom70 due to the inherent flexibility of the complex, as discussed above. However, we were able to fit the TPR4, TPR5, and TPR6[50] motifs of Tom70 into the cryo-EM density map, which are in proximity to the disordered C-terminal of EspB. This is in accordance with our structural observation because bacterial toxins or effector proteins typically interact with host-cell receptors through a specific subdomain or only a few amino acid residues within that subdomain. The heptameric EspB complex is a large Mtb effector protein that interacts with the TPR4–6 motifs of Tom70. Tom70 contains a large cytosolic domain and exists as a dimer, whereas the TPR4–6 motifs constitute only a small region in the upper portion of Tom70 that is responsible for EspB binding. In contrast, EspB forms a heptamer, and any one of its seven protomers can potentially interact with the two TPR4–6 motifs of the Tom70 dimer. Consequently, multiple combinations of interactions between the seven EspB protomers and the dimeric Tom70 are possible, giving rise to the different conformational states observed during 3D hetero-refinement. The upper region of Tom70 (251–431), which includes the TRP4-6 motifs[49,50], was specifically selected based on previous studies indicating that this region is involved in precursor protein recognition. Docking of this Tom70 region into the EM density map revealed a favourable fit without detectable clashes

(Fig. 4A and Supplementary Figure S**8B**). In parallel, fitting of the AlphaFold-predicted EspB (monomer) and Tom70 (251–431) yielded an EspB-Tom70 complex, which is similar to our rigid body structure that fitted well into our cryo-EM map (State 3) density map (Supplementary Figure **S8C** and **S8D**). To further validate the proposed docking rearrangement, residues at the EspB-Tom70 complex interface were evaluated. The key EspB residues identified are: D179 interacting with Tom70's Q315 (3.13 Å) and N277 (2.16 Å), and R69 most probably interacting with Tom70's N320 (2.69 Å) through hydrogen bonding (Fig. 4B and 4C-**Table 2**). Notably, these residues are conserved across homologs from multiple *Mycobacterium* species (Supplementary Figure **S8E**), supporting their functional importance in mediating EspB-Tom70 interaction.

To further evaluate and validate the contribution of these residues to EspB-Tom70 interactions, site-directed mutagenesis was performed in which D179 (acidic polar) and R69 (basic polar) were individually substituted with alanine (nonpolar and neutral). The effects of these substitutions were initially assessed using Microscale Thermophoresis (MST). Both R69A and D179A mutants exhibited markedly reduced binding affinity for Tom70, with values of 2.59 μM and 3.26 μM, respectively (Fig. 4D and 4F). These results indicate that the single mutants (R69A and D179A) bind Tom70 less efficiently than the wild-type protein. This finding suggests that these two residues play a significant role in the EspB–Tom70 interaction. Consistently, co-immunoprecipitation analysis was performed with these two mutants, which demonstrated complete abolition of the EspB-Tom70 association upon substitution of R69 relative to wild-type EspB, as detected by an anti-Tom70 antibody (Fig. 4E). Collectively, these findings establish a crucial role for R69 and D179 in stabilising the EspB-Tom70 interaction.

EspB's interaction with Tom70 disrupts mitochondrial homeostasis.

To investigate the cellular consequences of the EspB-Tom70 interaction, we employed *Saccharomyces cerevisiae* as our model organism because of its well-established resemblance to higher eukaryotes[51] and its ability to switch its metabolic dependency from fermentative media (dextrose) to respiratory media (glycerol) depending on available conditions[52]. As reported earlier, under respiratory media conditions, mitochondrial biogenesis and functions were highly upregulated. Thus, in our studies, we have overexpressed EspB and its corresponding mutants in BY4742 yeast cells and observed phenotypic changes by spot assays in both fermentative and respiratory media. Yeast cell growth was observed at both permissive and non-permissive temperatures. EspB overexpression caused a significantly greater growth defect in glycerol media than in dextrose across all temperature conditions. (Fig. 5A and Supplementary Figure **S9A**). However, yeast cell growth was similar to wild type (WT) in the mutated EspB (R69A and D179A). The overexpression of EspB and its respective mutants was validated via western blot analysis of yeast cell extracts probed with an anti-GFP antibody (Supplementary Figure **S3F**). To further investigate the effect of EspB on yeast cell death, EspB and its GFP-deficient mutant strains (Supplementary Table **S3**) were used. Yeast apoptotic progression is characteristically marked by phosphatidylserine externalisation and compromised plasma membrane integrity. These phenotypes are readily quantifiable by co-staining with fluorescein isothiocyanate (FITC)-labelled Annexin V and propidium iodide (PI)[51]. Flow cytometry analysis of EspB and its mutants on yeast cells revealed that the

majority of the EspB-expressing strains were in late apoptotic stages, accounting for ~ 75% of the cell population. However, the percentage of late apoptotic cells was lower in the single EspB mutants R69A and D179A (approx. 14–15 %) an a very small population of cells was found in either the early or late apoptotic quadrants in the double mutant R69A/D179 (Fig. 5B and Supplementary Figure **S9B**), which is similar to our wild-type. Hence, it is concluded that EspB promotes cell death via apoptosis. We next determine whether apoptosis is associated with mitochondrial dysfunction.

Initially, EspB-GFP and Tom70-mCherry partially colocalised when cultured in dextrose media. However, this localisation increased substantially in respiratory media (glycerol-containing media), as quantified using Pearson's correlation coefficient in ImageJ. Intriguingly, a reduction in localisation was observed in both single and double mutants of EspB (Fig. 5C). To further examine the implications of EspB and its mutants on mitochondrial integrity, we measured mitochondrial ATP production rate. Overexpression of EspB in cells led to a marked reduction in mitochondrial ATP levels, which were restored in the single and double mutants to levels comparable to those of the wild-type control. Although mitochondrial biogenesis is upregulated under respiratory media, it is well established that, under the influence of pathogenic toxins, mitochondrial ATP production is disrupted in cell mitochondria (Fig. 5D)[53]. Simultaneously, to assess mitochondrial integrity, we performed flow cytometry analysis to examine total mitochondrial function/potential using the TMRE dye. Surprisingly, yeast cells expressing EspB exogenously in glycerol media showed a significant reduction in mitochondrial membrane potential. This depolarising phenotype was independently validated using JC-1 dye, which showed an increased green-to-red fluorescence ratio indicative of mitochondrial depolarisation. In contrast, single and double mutants of EspB maintained a membrane potential similar to that of the wild-type (Fig. 5E and 5F).

Discussion

Intracellular pathogens have employed sophisticated mechanisms to manipulate and regulate host cellular pathways and establish a niche for survival and replication [2,3]. *Mycobacterium tuberculosis* (*Mtb*) is one such pathogen that evades host defence mechanisms by secreting virulence factors that interfere with phagosomal maturation and host defence signalling[3,15]. Among these, many toxins, such as EsxAB (ESAT-6-CFP10), are required for phagosomal membrane disruption. It binds to the TLR-2 receptor in macrophages, leading to suppression of innate immune signaling[43] and promoting host cell survival. In contrast, the Tuberculosis Necrotising toxin (TNT) induces host cell death by depleting NAD+ after its secretion [54,55]. Recent studies have shown that EspB is a crucial ESX-1 secreted PE/PPE substrate responsible for phagosomal rupture and mitochondrial damage [32,42,47,48] by interacting with the phospholipids phosphatidic acid (PA) and phosphatidylserine (PS) [32,42].

Furthermore, localisation of EspB at the sites of mitochondrial membrane damage suggests a direct role in mitochondrial targeting and damage. However, the relatively low abundance of these phospholipids in the mitochondrial outer membrane raised the possibility that receptor proteins mediate EspB binding to mitochondria, consistent with previous studies showing that a model membrane with a lipid composition

similar to the mitochondrial outer membrane remained intact after treatment with EspB [32,42]. Previously, several bacterial toxins, including pore-forming toxins and effector proteins, have been shown to interact with host membranes via specific membrane-associated receptors as well as lipid membranes [54,56–58]. As an example, *Helicobacter pylori* from the Type IV secretion system transports its oncogenic effector CagA by interacting with integrin a5β1 and promotes host signalling pathway dysregulation [59], and VacA binds with mitochondria, inducing cytochrome c release and mitochondrial depolarization[60,61]. Other species, such as cholera toxin from *Vibrio cholerae*, which uses the Type II secretion system, binds to the GM1 receptor of epithelial cells and promotes severe watery dysentery [62], and pneumolysin from *Streptococcus pneumoniae* induces mitochondrial fragmentation and depolarisation [63,64]. Therefore, EspB might similarly exhibit membrane-binding activity through the membrane as well as receptors; however, the contribution of host receptors to EspB-mediated membrane damage was completely unknown. Here, we identify a role for mitochondrial receptors in EspB-mitochondria interactions for the first time and provide strong evidence that the receptor plays a critical role in the initiation of EspB-mediated membrane damage. Consistent with these hypotheses, enzymatic digestion of outer mitochondrial proteins with proteinase K and trypsin significantly reduced EspB binding. These suggest that EspB requires both lipids and a receptor for binding to its host mitochondria. Using a co-immunoprecipitation assay of EspB and mitochondria, we identified Tom70 as the host receptor for EspB. Tom70 is a well-characterised outer mitochondrial membrane protein responsible for the recognition and import of precursor proteins and chaperone-bound cargos into mitochondria. Recent studies suggest that Tom70 plays a role in coordinating mitochondrial stress and host-pathogen interactions [46,52].

Thus, we selected Tom70 as the potential target for the EspB interaction. Multiple approaches, including size-exclusion chromatography (SEC) peak shift, microscale thermophoresis (MST), mass spectrometry and a cellular colocalisation assay, consistently supported the formation of the EspB-Tom70 complex. Structural characterisation using single-particle cryo-electron microscopy further revealed the overall architecture of the EspB-Tom70 complex, in which an additional density associated with the EspB oligomer, blocking the central hollow pore, was localised near the C-terminal disordered region of EspB. However, the intrinsic flexibility and conformational heterogeneity of Tom70 prevented high-resolution reconstruction of the complete complex. Similar challenges have previously hindered the structural characterisation of many protein complexes, despite advances in cryo-EM. Like in cholera toxin-GM1 complex[62], anthrax toxin receptors (ANTXR1-2) complex with protective antigen [65], *Staphylococcus* α-hemolysin and ADAM-10[58] due to positional variability. Recently, the structure of the GPCR-G protein-β-arrestin megacomplex faced a similar challenge in solving the high-resolution structure due to conformational heterogeneity [66]. Likewise, we are unable to determine the high-resolution structure of the EspB-Tom70 complex due to conformational heterogeneity. However, the observed conformational heterogeneity is expected, as EspB binds only to the TPR4–6 motifs of dimeric Tom70 rather than to its entire cytosolic domain. As a heptamer, EspB can engage the two TPR4–6 motifs through different protomers, generating multiple binding configurations that are captured as distinct conformational

states during 3D hetero-refinement. Although the structure is of low resolution, together with rigid-body docking studies and a structure predicted by AlphaFold, it suggests that residues R69 and D179 of EspB mediate the interaction with Tom70 through hydrogen bonding. However, site-directed mutagenesis of these residues was performed to validate the above observation, and it substantially impaired Tom70 binding, supporting our proposed structural model. Together, these findings suggest that EspB binds to Tom70 via hydrogen bonding, along with an outer membrane lipid component.

The physiological significance of the EspB-Tom70 interaction was analysed using yeast as our model organism, given its close resemblance to higher eukaryotes. The exogenous expression of EspB results in growth depletion in both fermentative (dextrose) and respiratory (glycerol) media, particularly under respiratory conditions where mitochondrial activity is essential for cellular survival. Importantly, site-directed mutagenesis of EspB residues in the EspB-Tom70 interface largely rescued these growth defects. Expression of EspB led to yeast cell death via apoptosis. To understand the role of mitochondria in these apoptotic yeast cell deaths, mitochondrial integrity was analysed. Many biochemical and biophysical experiments showed reduced ATP production and mitochondrial membrane depolarisation when EspB was expressed exogenously. However, mutations that disrupted EspB binding to Tom70 restored the mitochondrial function and integrity.

Based on our current findings, we propose a model in which EspB, following ESX-1-mediated secretion and phagosomal rupture, gains access to the host cytosol and subsequently targets mitochondria through cooperative interactions with mitochondrial phospholipids and the receptor Tom70, thereby affecting mitochondrial health by impairing ATP synthesis and mitochondrial membrane potential, which in turn activates apoptotic signalling pathways, leading to yeast cell death (Fig. 6). Previous reports have suggested that *Mtb* internalises within the phagosome and arrests phagosomal maturation using various toxins or effector proteins like ESAT6-CFP10 and EspB [32,67,68]. These effector proteins play a crucial role in rupturing the phagosome and releasing cellular materials in the cytosol, which leads to cell death of the macrophages [69,70] thus promoting bacterial dissemination and *Mtb* survival. The deletion of the RD1 locus involving many effector proteins in the BCG vaccine leads to the cessation of this pathway that arrests phagosomal release [69,71] and has been used as a therapeutic for a long time. Previous reports suggest that EspB also plays a crucial role in arresting IFN-γ-induced autophagy in murine macrophages[72]. Thus, it was hypothesised that EspB plays a dual role: first, it stops phagosomal maturation, and second, it escapes from the phagosome during phagosomal rupture and is released into the cytosol, where it comes into contact with mitochondria. It damages mitochondrial integrity, leading to cell death by apoptosis, which weakens host immunity and promotes the survival of *Mtb* in host cells.

Although our study provides the first mechanistic insight into the role of EspB in tuberculosis pathogenesis by targeting the mitochondrial receptor protein Tom70, several questions remain unanswered. Higher-resolution structural approaches will be necessary to define the organisation of the EspB-Tom70 complex, and the identification of additional residues may facilitate the development of therapeutic strategies to disrupt EspB-Tom70 recognition and limit mitochondrial damage during infection.

Materials and Methods

Cloning, expression and purification of WT EspB and its mutants

The wild-type EspB construct was obtained from Sengupta et al. (2023). Point mutants of EspB (R69A and D179A) were generated using site-directed mutagenesis using polymerase Chain Reaction (PCR) using primers as listed in Supplementary **Table 3** and cloned into the pET28a vector. The positive colonies were screened and verified by DNA sequencing. EspB WT and mutants were then transformed into *E. coli* BL21(DE3) cells for protein overexpression. The cells were grown in Luria Bertani (L.B) media at 37ºC until the O.D. $_{600}$ reached 0.6. Protein expression was induced with 0.5 mM Isopropyl β-D-1-thiogalactopyranoside (IPTG), and cultures were incubated at 16ºC for 12 hours. Cells were harvested by centrifugation and resuspended in lysis buffer containing 20 mM Tris-Cl, pH 8.5, 300 mM NaCl, 1 mM PMSF, and 10 mM imidazole. The resuspended cells were lysed by sonication (20kHz, 28% amplitude, 0.3 seconds ON and 0.6 seconds OFF cycle) and centrifuged at 13,000 rpm for 60 minutes at 4ºC. For affinity purification, the supernatant was incubated overnight with Nickel-Nitrilotriacetic Acid (Ni-NTA) agarose resin. The resin was extensively washed with buffer containing increasing concentrations of imidazole (10 mM, 20 mM, 40 mM, and 80 mM) to remove excess unbound proteins, followed by elution at 300 mM imidazole. The eluted fractions were concentrated using 10 kDa centrifugal filters, followed by Size-Exclusion Chromatography (SEC) using a Superdex 200 Increase 10/300 GL column on an AKTA-FPLC system to separate the monodisperse oligomeric species. SEC was performed using a 20 mM Tris-Cl buffer, pH 7.5, and 150 mM NaCl. The heptameric assembly was concentrated and run on a 15% SDS gel alongside a protein marker to confirm its purity.

Mitochondrial lysate preparation

The mitochondrial isolation protocol from Saccharomyces cerevisiae was performed with slight modifications [71–73]. WT and EspB-GFP-tagged yeast cultures were cultured in respiratory dropout media and harvested at 6000 rpm for cell wall digestion. The cells were resuspended in 100 mM Tris-H_2SO_4 (pH 9.4) buffer containing 10 mM dithiothreitol (DTT) at 0.5 g wet weight/mL and incubated at 25°C for 20 minutes with gentle shaking (70 rpm). Following this, cells were harvested and washed with 1.2 M sorbitol. Subsequently, the cells were resuspended in zymolase buffer (1.2 M sorbitol, 20 mM KH_2PO_4, pH 7.4) to a final pellet wet weight of 1.5 g. Zymolase (according to pellet weight) was added, and the suspension was incubated at 25°C with gentle shaking to generate spheroplasts. Spheroplast formation was confirmed microscopically using 0.1% SDS and 1.2 M sorbitol. The resulting spheroplasts were harvested by centrifugation (5000 rpm) and washed once with 1.2 M sorbitol. For homogenisation, spheroplasts were gently resuspended in pre-cooled homogenisation buffer (0.6 M sorbitol, 10 mM Tris-Cl, pH 7.4, 0.2% BSA, 1 mM PMSF). Under ice-cold conditions, the suspension was mechanically lysed by 30 + 20 strokes in a Dounce homogeniser. Mitochondria were then isolated, using differential

centrifugation. The homogenate was first centrifuged at 3000 rpm to pellet cell debris, and the supernatant was centrifuged at 15,000 rpm in an oakridge tube to obtain a crude mitochondrial pellet. The pellet was resuspended in 1ml of homogenisation buffer and purified by alternating centrifugation steps (5000 rpm and 14,000 rpm) to remove contaminating debris. Finally, the purified mitochondria pellet was resuspended in 0.5 – 0.3 ml of SEM buffer (10 mM MOPS KOH, pH 7.2, 250 mM sucrose, 1 mM EDTA), snap-frozen in liquid nitrogen, and stored at -80°C until further use.

Mitochondrial Sedimentation Assay

To evaluate the association between EspB and mitochondria, purified EspB and isolated mitochondria were mixed in a 1:4 molar ratio and incubated at 4º C for 1, 2 and 4 hours. Following incubation, the samples were centrifuged at 13000 rpm for 30 minutes to separate mitochondrial-associated EspB (pellet) from unbound EspB (supernatant). The supernatant and pellet were collected separately at each time interval, and the pellet fractions were resuspended in SEC buffer (10 mM Tris, pH 7.5 and 150 mM NaCl). The samples were then run on a 12% SDS gel. Precision Plus™ Dual colour marker was used as a molecular weight standard in all further experiments. The samples were further analysed by western blot using an anti-His antibody (details provided in Supplementary **Table 5)** to detect EspB.

Western blot analysis

The separated proteins from SDS PAGE were transferred onto a PVDF membrane using an electroblotting apparatus in 1X Tris-Glycine-Methanol transfer buffer. Following transfer, the membrane was blocked with 5% skimmed milk for 1 hour, then washed in 1X TBST (Tris-buffered saline with 0.1% Tween-20). The target protein was then identified by incubation with the respective primary antibody, followed by washes with 1X TBST. Signal amplification was achieved by incubating the blot with HRP-conjugated anti-rabbit/mouse secondary antibodies (1:10000) for 1 hour, followed by TBST washes. Detection was finalised by adding Luminol-based chemiluminescent substrate and exposing the membrane to X-ray films. A similar method was used in all future experiments.

Enzymatic treatment of Mitochondria and binding analysis with EspB:

Isolated mitochondria were pelleted to remove the SEM buffer and resuspended in 10 mM Tris, pH 7.5, and 150 mM NaCl, followed by treatment with Proteinase K (50 µg/ml) and Trypsin (40 µg/ml), respectively. After 10 minutes of incubation on ice, the samples were treated with 1 mM PMSF to inhibit the reaction. The samples were centrifuged at 4°C at 14000 rpm for 10 minutes to separate the cleaved protein fragments from the intact mitochondria, excluding the outer membrane proteins. The pellet was then resuspended in Tris buffer, pH 7.5 (as mentioned above), and incubated with EspB at a 1:4 molar ratio for 1 hr at 4ºC with gentle shaking. The samples were then centrifuged at 13000rpm for 30

minutes. The pellet and supernatant were collected separately, run on a 12% SDS-PAGE, and analysed using an anti-His antibody. The remaining samples were used for NS-TEM analysis.

Co-immunoprecipitation assay

Isolated mitochondria (2 mg/ml) were solubilised in 1 ml of lysis buffer (25 mM Tris-HCl, pH ~ 7.5, 50 mM KCl, 50 mM EDTA, 10% glycerol, 1% digitonin and 1 mM PMSF). After centrifugation at 14000 rpm for 15 minutes to isolate the solubilised fraction, the supernatant was diluted with 250 µl of detergent-free buffer. Simultaneously, 0.5 mg/ml of EspB was incubated with Ni-NTA beads preconjugated with 1.2 µl of anti-6X Histidine antibody. After an overnight incubation, the samples were centrifuged at 2,500 rpm for 5 minutes to remove the unbound EspB. The pellet containing the Ni-NTA beads attached to the 6X-His antibody and the EspB protein was incubated with solubilised mitochondrial lysate for 4 hrs at 4°C. The resulting immune complexes were subjected to three wash cycles with 1 ml of wash buffer (0.25% digitonin) to remove non-specific interactors. SDS loading dye was added to the pellet containing mitochondrial proteins interacting with an EspB-tagged His antibody bound to Ni-NTA beads, and the mixture was heated at 55°C for 10 minutes. The samples were resolved using SDS-PAGE, and subsequently analysed by western blotting using the primary antibodies listed in Supplementary Table 5.

Cloning, expression and purification of Tom70

The Tom70 gene was PCR-amplified using the primers listed in Supplementary Figure **Table 3** and cloned into the pET28a vector. The positive clone was confirmed by DNA sequencing and subsequently transformed into *E. coli* (DE3) BL21 cells for overexpression. The transformed cells were grown at 37ºC until an O.D.600 of 0.6, then induced for protein expression with 1 mM IPTG for 22 hours. Cell harvesting was performed by centrifugation, and the cells were resuspended in a lysis buffer containing 20 mM Tris-Cl, pH 7.5, 100 mM NaCl, 10% glycerol, 0.2mg/ml Lysozyme, 1 mM PMSF, 0.51 mM DDM, and 10 mM Imidazole. The resuspended cells were lysed by sonication (0.3 second ON; 0.6 second OFF, 28% Amp.). Cell debris was removed by centrifugation at 13,000rpm for 60 minutes at 4ºC. Protein was purified using Ni-NTA affinity chromatography. Therefore, the supernatant was collected after centrifugation and incubated overnight with Nickel-Nitrilotriacetic Acid (Ni-NTA) beads. The protein was subjected to sequential washes at 10 mM, 20 mM, 40 mM, and 60 mM imidazole, each supplemented with 0.51 mM DDM, followed by elution at 300 mM Imidazole and 0.085 mM DDM. The eluted fractions were concentrated using an Amicon concentrator with a molecular cut-off of 10 kDa (MWCO) before being injected into the Size Exclusion Chromatography (SEC) S200 Increase 10/300 GL column on an AKTA-FPLC system. The SEC was performed using a 20 mM Tris-Cl buffer, pH 7.5, 150 mM NaCl and 0.085 mM DDM. The samples were loaded onto a 12% SDS gel to assess the protein's purity. **Mass spectrometry analysis of Tom70**

For Tom70 identification, protein bands were excised from the gel and fragmented into fine pieces. The gel pieces were washed twice with 400 µL of double-distilled water for 15 minutes each. Subsequently, the gel pieces were then incubated in 400 µL of acetonitrile for 10 minutes. After removal of the supernatant, the gel pieces were dried, and 100 µL of 10 mM dithiothreitol (DTT) prepared in 100 mM

Ammonium Bicarbonate (ABC) was added. The samples were incubated for 45 minutes at 55ºC to reduce disulfide bonds. Following reduction, the DTT solution was discarded, and 100 µL of 55 mM Iodoacetamide prepared in 100 mM ABC was added. The gel pieces were incubated in the dark at room temperature for 30 minutes for alkylation. After removing the alkylation solution, the gel pieces were washed twice with gel wash solution containing 50% (v/v) acetonitrile, 25 mM ABC for 15 minutes each. The supernatant was discarded, and the gel pieces were dehydrated with 400 µL of 100% acetonitrile for 10 minutes, then dried. For in-gel digestion, the dried gel pieces were treated with a trypsin working solution containing 20 µg/mL sequencing-grade modified Trypsin, prepared in 25 mM ABC, and incubated overnight at 37ºC. After digestion, the supernatant containing peptides (S1) was collected and stored separately. Peptides remaining in the gel pieces were extracted using an extraction buffer containing 50% acetonitrile and 0.1% trifluroracetic acid (TFA), followed by sonication in a water bath sonicator for 10 minutes. The extracted supernatant was collected and pooled with the previously trypsin-digested supernatant (S1). The combined peptide solution was concentrated using a high-speed vacuum concentrator. The concentrated samples were mixed in a 1:1 molar ratio with a-cyano-4-hydroxycinnamic acid (HCCA) and spotted onto a MALDI plate. Mass spectrometric analysis was performed using a rapifleX MALDI-TOF/TOF mass spectrometer operated in positive-ion reflectron mode with FlexControl software. The acquired peptide's m/z values and their intensities were analysed using Mascot for protein identification.

Mass spectrometry analysis of EspB and co-immunoprecipitation samples.

For peptide analysis of EspB and co-immunoprecipitation samples, proteins were reduced using 100 mM Ammonium Bicarbonate and 100 mM DTT, followed by incubation in a dry bath at 57ºC for 30 minutes. Alkylation of cysteine residues was performed by adding 100 mM iodoacetamide and incubating in the dark at RT for 20 minutes. The samples were then subjected to proteolytic digestion with a 20 µg/mL solution of sequence-grade modified Trypsin and incubated overnight at 37ºC. Before sample loading, the V tip or Z tip columns were sequentially preequilibrated with 100%, 80%, and 2% methanol by centrifugation at 2000 rpm/minute, with each equilibration step repeated three times. The trypsin-digested samples were acidified with methanol, acetonitrile and 0.1% TFA and loaded onto the preequilibrated columns. Multiple loading and washing cycles were performed using 2% acetonitrile and 10% TFA to remove salts and contaminants. Bound peptides were subsequently eluted using 50% and 80% acetonitrile by centrifugation at 2000 rpm/minute. The samples were then dried in a vacuum concentrator. Peptide analysis was performed using an LC-MS Orbitrap fusion mass spectrometer coupled to a nano-liquid chromatography system. Peptides were separated on a reverse-phase C-18 analytical column (15 cm length, 1.5 µm particle size, internal diameter 150 µm) using a linear gradient of 2–90% acetonitrile containing 0.1% formic acid. The eluted peptides were analysed by mass spectrometry using a nano-electrospray ionisation source operating in positive-ion mode. Data acquisition was performed in data-dependent acquisition (DDA) mode, which automatically switches between MS and MS/MS analysis of the most abundant precursor. Full-scan MS spectra were recorded in the Orbitrap mass analyser over a m/z range of 350–2000 with an ion intensity threshold of 5000 counts. The 20 most intense precursor ions with charge states + 2 to + 8 were selected for

fragmentation and MS/MS analysis in the ion trap mass analyser. Fragmentation was achieved using higher-energy C-trap dissociation (HCD) with a normalised collision energy of 30%. The raw mass spectrometric data were processed and analysed using Proteome Discoverer 2.5. Protein identification was based on high peptide-spectrum match (PSM) scores and high sequence coverage; the selected proteins are shown in Figure **Table 1** and Supplementary Figure **S1E, S2C-D.**

Analysis of EspB-Tom70 complex formation by SEC

The purified EspB and Tom70 were mixed in a 1:2 molar ratio and incubated for 30 minutes at 4ºC. Following incubation, the complex was subjected to SEC (AKTA-FPLC, GE Healthcare) using a buffer composition of 20 mM Tris (pH 7.5) and 150 mM NaCl. The elution profile of the EspB-Tom70 mixture was compared with those of EspB and Tom70 individually. Formation of the EspB-Tom70 complex was assessed by detecting an additional peak corresponding to higher-molecular-weight species, distinct from the peaks of the individual proteins. Fractions corresponding to the EspB-Tom70 complex peak were collected and analysed by 12% SDS-PAGE, and the presence of both EspB and Tom70 bands in the same SEC fraction confirmed co-elution of the proteins, indicating complex formation.

Microscale thermophoresis (MST) analysis of WT EspB and its mutants with Tom70

MST determined the binding affinity of the EspB-Tom70 complex. WT EspB was fluorescently labelled with RED-NHS, a second-generation amine-reactive dye (Nanotemper). The labelled WT EspB was diluted to a final concentration of 10 nM using a buffer containing 20 mM Tris (pH 7.5), 150 mM NaCl, and 0.05% Tween 20. For affinity measurements, labelled WT EspB was mixed with a 16-fold serial dilution of Tom70, starting at an initial concentration of 4.25 µM, prepared in buffer containing 20 mM Tris and 150 mM NaCl. The same buffers are used for all subsequent dilutions. After incubation for 30 minutes on ice, the samples were loaded into MST Monolith NT.115 capillaries (used for all runs) and analysed using a Monolith NT.115 pico instrument using MO. Control software[73] at RT (LED/Excitation settings 20%, MST power 40%).

For the EspB D179A mutant, the final concentration of the fluorescently labelled protein was maintained at 10nM, mixed with serially diluted Tom70 (initial concentration 2.13 µM), and analysed using MO. Control software at RT (Excitation settings 5% and MST power 40%). The Fnorm and ligand concentration data were plotted using Excel. 3 data points out of 32 was removed to improve the curve fit.

Similarly, for the R69A mutant of EspB, the final concentration was 10 nM, mixed with serially diluted Tom70 (initial concentration 4.25 µM), and analysed using MO. Control software at RT (Excitation settings 5% and MST power 40%). The Fnorm vs ligand concentration data were plotted in Excel. 3 data points out of 32 was removed to improve the curve fit.

All binding assays were performed using two independent purification batches of each sample. The obtained data points were analysed using MO. Affinity analysis software version 2.2.5 [74]. Equilibrium dissociation constant (k_d) was calculated by fitting the normalised fluorescence changes to the K_d model.

Negative stain – Sample preparation, Imaging and data processing

Sample preparation

For EspB-Mitochondria complex formation, purified EspB was mixed with WT mitochondria and enzymatically treated mitochondria at a 1:2 molar ratio, incubated on ice for 1hour, and then imaged.

For the analysis of the EspB-Tom70 complex following SEC, fractions corresponding to peaks 1, 2, and 3 were collected and diluted to a final concentration of 0.025mg/mL before freezing.

The copper grids were glow-discharged for 30 seconds at 20 mA using a GloQube glow discharge system. Subsequently, 3.5 µL of the abovementioned samples was applied to fresh, glow-discharged grids. An extra buffer was removed using a Whatman filter paper, followed by negatively staining with 1% (w/v) uranyl acetate and blotting off the excess staining solution. The stained grids were air-dried before imaging.

Data Imaging

Dried grids were imaged using a 120kV Talos L120C transmission electron microscope (TEM), equipped with a (4K x 4K) Ceta camera. Micrographs were collected at 73000x magnification with a calibrated Å/pixel value of 1.92. Images were acquired from two independent purifications.

Image processing and analysis

For the analysis of EspB binding to WT and enzymatically treated mitochondria, a total of 40 micrographs were collected from two independent purifications. The NS-TEM raw micrograph was imported into EMAN 2.1[75], and EspB particles associated with mitochondria were manually picked from each set. For quantitative analysis, 12 medium-sized mitochondria were selected from each condition, and the number of particles was determined using e2boxer.py. The same procedure was used for all the samples. The data was then analysed using GraphPad Prism 8.4[76].

For the analysis of the EspB-Tom70 complex by SEC, a total of 30 micrographs were collected for each SEC peak fraction (Peak 1, 2, and 3) to assess morphology within the respective fractions.

Cryo-EM sample preparation, data collection and processing

Sample preparation

For cryo-EM analysis of the EspB-mitochondria complex, purified EspB was mixed in a 1:4 molar ratio with WT mitochondria and enzymatically treated mitochondria and incubated for 1 hour on ice before vitrification using a FEI Vitrobot Mark IV plunger. 3 µl of sample was applied to a freshly glow-discharged (20 mA, 90 seconds) R 1.2/1.3 300-mesh copper Quantifoil grid, and the excess sample was blotted off for 6 seconds at a blot force of + 10, followed by plunge-freezing in liquid ethane surrounded by liquid nitrogen.

For EspB alone, 3 µl of purified EspB (2mg/ml) mixed with 0.03% fluorinated octyl maltoside (FOM) was added to R1.2/1.3 300 mesh Quantifoil grids. Excess sample was removed by blotting for 6.5 seconds at a blot force of + 7, followed by plunge-freezing in liquid ethane.

For the EspB-Tom70 complex, purified EspB and Tom70 were mixed at a 1:10 molar ratio and incubated on ice for 1 hour before freezing. Subsequently, 3 µl of the sample was applied to the freshly glow-discharged R1.2/1.3 300-mesh copper Quantifoil grid, and the excess sample was removed by blotting off for 6.5 seconds at a blot force of + 10, followed by plunge-freezing in liquid ethane surrounded by liquid nitrogen. All vitrified grids were stored in liquid nitrogen until data collection.

Data imaging

The grid was then inserted for Cryo-EM data collection into a 200kV Talos Arctica TEM equipped with a K2 Summit Direct Electron Detector (4K x 4K). Automated data were collected using LatitudeS software[77], and image acquisition was controlled using Digital Micrograph GMS version 3.5 (Gatan Inc.). All data were collected at 54,000x magnification, calibrated with an Å/pixel value of 0.92. The abovementioned protocol was followed for all the samples.

For WT and enzymatically treated mitochondria with the EspB sample, data were collected in counting mode with a final dose of 43 $e^{-}/Å^{2}$. Data were collected from two independent purifications. A total of 2197, 46 and 20 were collected for EspB with WT mitochondria, proteinase K-treated mitochondria, and trypsin-treated mitochondria, respectively. 4107 micrographs were collected for EspB at a final electron dose of 40 $e^{-}/Å^{2}$ and 40918 micrographs were collected for the EspB-Tom70 complex sample at an electron dose of 52 $e^{-}/Å^{2}$.

Data Processing

For the EspB-mitochondria data set, 2197 micrographs were imported to Cryosparc 4.5. Beam-induced motion and gain normalisation were performed using the Patch Motion Correction module, followed by Contrast Transfer Function (CTF) correction using Patch CTF estimation. A total of 1,292,323 particles were automatically picked using the Blob Picker with higher normalised cross-correlation (NCC) and lower histogram threshold parameters and extracted with a 280-pixel box size. Several rounds of reference-free 2D class averaging were performed to remove the junk particles. The best quality 2D classes comprising 13,439 particles were selected and are shown in Supplementary Figure **S2B**.

For the EspB-only dataset, 4107 micrographs were imported into cryoSPARC 4.5 and subjected to beam-induced motion and gain correction using Patch Motion Correction and CTF correction using Patch Ctf estimation. The micrographs were curated based on exposure and estimated resolution, applying a resolution cut-off of 6 Å and around 3623 best micrographs were selected for further processing. Particles were picked using a Blob Picker with high NCC and lower histogram values. A total of 1738,968 particles were picked and extracted using a box size of 240 pixels. Multiple rounds of 2D class averaging were performed to remove junk and poorly aligned particles, and the best 2D classes, containing 360,101 particles, were selected for three-dimensional (3D) heterorefinement with C7 symmetry imposed. An ab initio reconstruction generated from the selected 2D class averages, together with the map from the previous study (**EMDB:34878**) filtered to 40 Å resolution, was used as a reference for heterorefinement. The particles were divided into 6 classes, and the best classes with 302017 particles were selected for final Non-Uniform Refinement followed by Local Refinement. For map enhancement, the final reconstructed map was run in DeepEMhancer. The global resolution of the final reconstruction was estimated using the gold-standard Fourier Shell Correlation (FSC) at a threshold of 0.143. The local resolution estimation was performed using the local resolution estimation interface in cryoSPARC. The data were displayed using different surface colours based on local resolution, as shown in UCSF ChimeraX[78] for representation in Supplementary Figure **S5**. The structural comparison between previously reported structures and our model was performed using the MatchMaker tool in UCSF ChimeraX[78].

For the EspB-Tom70 complex dataset analysis, 40,918 micrographs were imported into cryoSPARC 4.5, and beam-induced motion correction followed by CTF estimation was performed using a workflow similar to that described above. Following exposure-based micrograph curation, 35278 micrographs were used for further analysis. Around 10,559,579 particles were picked using a Blob Picker with high NCC and low threshold parameters. After multiple rounds of 2D classification, 391,262 particles were finally selected for heterogeneous refinement using C1 symmetry and divided into 4 classes. The previously reported EspB density map (EMDB:34878), low-pass-filtered to 40 Å, was used as a reference. The resulting classes showed conformational heterogeneity and were further subjected to Non-Uniform Refinement followed by Local Refinement, as shown in Fig. 3F.

The best map, with 129,031 particles, was processed further using DeepEMhancer, as shown in Fig. 3E. The overall resolution was calculated using gold standard FSC criteria at a 0.143[79] threshold. The Local resolution estimation was performed using cryoSPARC and depicted using surface colouring in UCSF ChimeraX[78].

Model building and refinement of EspB only

Previously reported X-ray structure of EspB (PDB ID 6XZC[80]) was fitted into the cryo-EM density map of EspB using rigid-body fitting in UCSF ChimeraX[78]. The fitted model was refined using Phenix. Further, model building and manual adjustments were performed in Coot[81], and regions showing positional

shifts were manually corrected to optimise the fit to the Cryo-EM density. The refined model was subjected to real-space refinement using Phenix. The final refined EspB atomic model was validated using map-to-model FSC statistics in Phenix [72] and UCSF ChimeraX [78]

Construction of yeast strains and plasmids by genetic technology

The *Saccharomyces cerevisiae* strains used in this study, listed in Supplementary Table S4, are based on the BY4742 haploid Mat-α background. All primer sequences used for PCR amplification and vectors used for cloning are listed in Supplementary Table **S3**. The Tom70 gene was amplified from yeast genomic DNA and cloned into the centromeric vector $pRS416_{TEF}$, which carries a mCherry tag. Similarly, the EspB gene was amplified from the clone used in the previous study [42] and cloned into the empty vectors pRS415TEF and pRS413ADH, as well as into the same vectors containing the GFP tag. Mutations such as R69A and D179A in the EspB protein were randomly mutagenised and cloned into both $pRS415_{TEF}$ and $pRS413_{ADH}$, each with a GFP tag as well as $pRS415_{TEF}$ empty vector (for fluorometric assays), using BamH1/Sal1. Subsequently, the EspB and its mutants' clones, along with the Tom70-mCherry clone, were transformed into WT using the lithium acetate (LiAc) method [82].

Growth media conditions of yeast cells

S. cerevisiae cells were either grown in (i) Synthetic complete dropout (leucine, uracil, histidine or both uracil and histidine) media *i.e.* SCD-Leu, SCD-Ura, SCD-His or SCD-Ura-His media containing yeast nitrogen base without amino acids (0.67%), leucine dropout supplement (0.069%), uracil dropout supplement (0.069%), histidine dropout supplement (0.069%) or double dropout supplement (0.072%) along with dextrose, glycerol and lactate (2%) or (ii) YPG media containing yeast extract (1%), peptone (2%), glycerol (2%). For growth on plates, 3% agar was added to the media. Cells were grown overnight at 30°C and shifted to fresh media. Cells were allowed to reach the exponential growth phase for all experiments.

Yeast viability assay (Spot test)

The respective yeast strains with the endogenous expression of the EspB plasmid and its mutants were grown overnight in their respective dropout media for spot analysis. Total yeast cells were grown to an OD600 of 0.5 and harvested at mid-log phase. The cells were resuspended in sterile water and subjected to 10-fold serial dilutions. Each dilution was spotted onto the respective media plates containing dextrose and glycerol media, and incubated at 30°C, 37°C, and 24°C for 36–180 hours.

Apoptotic assay by FITC Annexin V and PI staining

Apoptosis was determined using the FITC AnnexinV apoptosis detection kit, from an adapted protocol [83]. Wild-type yeast cells expressing empty vector, the EspB-His tag, and its mutants (without the GFP tag) were washed in sorbitol buffer (1.2 M sorbitol, 35 mM potassium phosphate, 0.5 mM $MgCl_2$, pH 6.8) and

digested with 15 U/ml zymolase at 28°C for 2 hours. Yeast cells were then harvested, washed with annexin binding buffer and resuspended in the same buffer with 2 µl of FITC Annexin V and 2 µl of propidium iodide (PI). Samples were incubated at room temperature for 30 minutes before being subjected to Flow cytometry analysis.

Colocalisation studies using confocal microscopy

The EspB gene and its mutants, such as R69A, D179A, and R69A/D179A, were amplified from the clone used in Sengupta et al [42]. They were constructed in the C-terminus region of $pRS413_{ADH}$ with a GFP tag. The Tom70 gene was amplified from the yeast BY4742 genome. The amplified gene was cloned into the $pRS416_{TEF}$ vector, which carries an mCherry tag at its C-terminus. Tom70-mCherry $pRS416_{TEF}$ and EspB-GFP $pRS413_{ADH}$ (including the mutants R69A and D179A-GFP $pRS413_{ADH}$ were transformed into the WT strain to visualise mitochondrial and EspB morphology and distribution, respectively. Tom70-mCherry specifically localises to mitochondria, enabling visualisation of mitochondrial morphology. Whereas EspB-GFP was used to observe the toxin's localisation inside the cell. The cells were harvested at mid-log phase (OD_{600} ~ 0.5) and imaged using an Olympus Fluoview 3000 confocal microscope with a 100X objective lens. The $\lambda_{EX}/\lambda_{EM}$ for GFP was 488/533 nm and for mCherry 587/610 nm, respectively. Subsequently, the images were processed using CellSens software, and the colocalisation was analysed using Pearson's coefficient plugins named JaCOP plugin in ImageJ.

ATP Assay

Total mitochondrial ATP production was measured using the Mitochondrial ToxGlo Assay kit. 100 µg of isolated mitochondria from yeast cells expressing EspB and its mutants, resuspended in SEM buffer, were frozen and thawed in liquid nitrogen for 3 cycles and incubated at 26°C for mitochondrial lysis. The samples were centrifuged at 14,000 rpm for 15 minutes to remove the SEM buffer. The mitochondrial pellet was resuspended in ATP assay buffer, and the ATP detection buffer was added. The mixture was incubated for 10 seconds in the TECAN microplate reader under shaking conditions, and fluorescence readings were collected in EXCEL software with excitation and emission wavelengths of 485/520 nm.

Fluorometric Analysis

To measure total functional mitochondrial mass, we used TMRE (Tetramethyl rhodamine ethyl ester), a mitochondrial membrane potential probe, and JC-1, a mitochondrial membrane potential probe. Exogenously expressed EspB and its mutants (in pRS413 without a tag) in yeast were grown to the early log phase (OD_{600} of 0.2–0.3). The cells were then washed once with 1X PBS, followed by staining with 8.75 µM JC-1 for 15 minutes and 5 µM JC-1 for 30 minutes in the dark at 25°C to detect the total functional mitochondrial mass. The cells were then pelleted, dissolved in 1X PBS, and analysed by flow cytometry on a Beckman Coulter Cytoflex flow cytometer. The excitation/emission wavelengths used for TMRE and JC-1 were 549/575 nm and 590 nm, respectively. 10,000 events were recorded for each sample, and the data were analysed using CytExpert software. For TMRE, we obtained relative median

fluorescence values, which were represented as bar graphs, by quantifying the fold change in median fluorescence intensity of the EspB and its mutant strains. Similarly, the JC-1 dye quantified the ratio of potential to non-potential mitochondria, with the graphs showing the JC-1 red and green percentages relative to the unstained samples.

Statistical analysis

Protein band intensities were quantified using MultiGauge software. Subsequent data analysis and statistical tests were performed in Excel (Microsoft) and GraphPad Prism 8.2.4 [76], respectively. For the colocalisation analysis, ImageJ [84] with JaCOP plugins was used to measure PCC (Pearson's correlation coefficient). All the statistical analyses were performed using unpaired one-way and two-way analysis of variance (ANOVA) (with multiple comparisons). All quantitative data were obtained from at least three independent experiments, and error bars represent the standard error of the mean (SEM). Asterisks denote the following levels of significance: *, $p \leq 0.05$; **, $p \leq 0.01$; ***, $p \leq 0.001$; ****, $p \leq 0.0001$.

Declarations

Acknowledgment

SD acknowledge Science and Engineering Research Board, India (Grant No. CRG/2022/002674) for financial support and DBT-BUILDER Program (BT/INF/22/SP22844/2017) and DST-FIST (SR/FST/LSII-039/2015) for the National Cryo-EM facility at IISc, Bengaluru. DM acknowledges the fellowship from the Ministry of Education (MoE), India, as a PhD scholar (JRF/SRF). SD and DM acknowledge the high-performance computing cluster "Beagle" at the Biological Sciences Division, IISc. We thank the LC-MS and SPR facilities, Division of Biological Sciences, Indian Institute of Science. We thank Mr Drose Ignatious Shane and Ms Keerthana H.S. for their help with Cryo-EM and TEM data acquisition. PDS and AC acknowledge the support by the Anusandhan National Research Foundation (ANRF) (ANRF/ARG/2025/001223/LS) and the Department of Science and Technology (DST-FIST Program-Phase III, no. SR/FST/LSII-045/2016-G). AC acknowledges the fellowship from the Department of Biotechnology, India, as a PhD scholar (DBT-JRF/SRF). PDS and AC extend their gratitude to Prof. Elizabeth A. Craig (University of Wisconsin-Madison, USA) for providing the anti-Tom70 and porin antibodies, and sincerely acknowledge the Department of Biochemistry for the Confocal Imaging and BD Cytoflex FACS facility, both within the Division of Biological Sciences, Indian Institute of Science.

Data availability:

The electron density maps were deposited in the Electron Microscopy Data Bank (EMDB) with the following accession codes: EspB-80893, EMDB-81473 for EspB-Tom70 state1, EMDB- 81461 for EspB-Tom70 state2, EMDB-81462 EspB-Tom70 state3 and EspB-Tom70 rigid dock. The coordinate files for the EspB model were submitted to the Protein Data Bank (PDB) under the data identifier PDB:26UN.

Authors Contribution

SD initial conceptualisation, DM, AC (Aishita), PDS and SD designed experiments, DM and AC (Aishita) generated the clones and protein purification, DM and AC (Aishita) did biophysical experiments, DM and SD did TEM based experiments, DM, AC (Arnab) and SD Cryo-EM studies-data acquisition and processing, AC (Arnab) did model building, AC (Aishita) and PDS did the mitochondria and yeast cell assays, DM, AC (Aishita), PDS and SD wrote and reviewed the manuscript.

Conflict of Interest

The authors declare no conflict of interest.

References

1. World Health Organisation (2024). Global Tuberculosis Report.
2. Brennan, P.J., and Nikaido, H. (1995). THE ENVELOPE OF MYCOBACTERIA. Annu. Rev. Biochem. *64*, 29–63. https://doi.org/10.1146/annurev.bi.64.070195.000333.
3. MacGregor, R.R. (1993). Tuberculosis: From history to current management. Semin. Roentgenol. *28*, 101–108. https://doi.org/10.1016/S0037-198X(05)80099-9.
4. Jarlier, V., and Nikaido, H. (1994). Mycobacterial cell wall: Structure and role in natural resistance to antibiotics. FEMS Microbiol. Lett. *123*, 11–18. https://doi.org/10.1111/j.1574-6968.1994.tb07194.x.
5. David N McMurray (1996). Mycobacteria and Nocardia. In Medical Microbiology, Baron Samuel, ed. (University of Texas Medical Branch at Galveston).
6. Forrellad, M.A., Klepp, L.I., Gioffré, A., y García, J.S., Morbidoni, H.R., de la Paz Santangelo, M., Cataldi, A.A., and Bigi, F. (2013). Virulence factors of the Mycobacterium tuberculosis complex. Virulence *4*, 3–66. https://doi.org/10.4161/viru.22329.
7. Green, E.R., and Mecsas, J. (2016). Bacterial Secretion Systems: An Overview. Microbiol. Spectr. *4*, 10.1128 /microbiolspec.vmbf-0012–2015. https://doi.org/10.1128/microbiolspec.vmbf-0012-2015.
8. Chiaradia, L., Lefebvre, C., Parra, J., Marcoux, J., Burlet-Schiltz, O., Etienne, G., Tropis, M., and Daffé, M. (2017). Dissecting the mycobacterial cell envelope and defining the composition of the native mycomembrane. Sci. Rep. *7*, 12807. https://doi.org/10.1038/s41598-017-12718-4.
9. Cole, S.T., Brosch, R., Parkhill, J., Garnier, T., Churcher, C., Harris, D., Gordon, S. V., Eiglmeier, K., Gas, S., Barry, C.E., et al. (1998). Deciphering the biology of Mycobacterium tuberculosis from the complete genome sequence. Nature *393*, 537–544. https://doi.org/10.1038/31159.
10. Houben, E.N.G., Korotkov, K. V., and Bitter, W. (2014). Take five — Type VII secretion systems of Mycobacteria. Biochimica et Biophysica Acta (BBA) - Molecular Cell Research *1843*, 1707–1716. https://doi.org/10.1016/J.BBAMCR.2013.11.003.
11. Phan, T.H., Ummels, R., Bitter, W., and Houben, E.N.G. (2017). Identification of a substrate domain that determines system specificity in mycobacterial type VII secretion systems. Sci. Rep. *7*, 42704.

https://doi.org/10.1038/srep42704.

12. Abdallah, A.M., Bestebroer, J., Savage, N.D.L., de Punder, K., van Zon, M., Wilson, L., Korbee, C.J., van der Sar, A.M., Ottenhoff, T.H.M., van der Wel, N.N., et al. (2011). Mycobacterial Secretion Systems ESX-1 and ESX-5 Play Distinct Roles in Host Cell Death and Inflammasome Activation. The Journal of Immunology *187*, 4744–4753. https://doi.org/10.4049/jimmunol.1101457.
13. Houben, E.N.G., Bestebroer, J., Ummels, R., Wilson, L., Piersma, S.R., Jiménez, C.R., Ottenhoff, T.H.M., Luirink, J., and Bitter, W. (2012). Composition of the type < scp>VII</scp> secretion system membrane complex. Mol. Microbiol. *86*, 472–484. https://doi.org/10.1111/j.1365-2958.2012.08206.x.
14. Simeone, R., Bobard, A., Lippmann, J., Bitter, W., Majlessi, L., Brosch, R., and Enninga, J. (2012). Phagosomal Rupture by Mycobacterium tuberculosis Results in Toxicity and Host Cell Death. PLoS Pathog. *8*, e1002507. https://doi.org/10.1371/journal.ppat.1002507.
15. Stanley, S.A., Johndrow, J.E., Manzanillo, P., and Cox, J.S. (2007). The Type I IFN Response to Infection with *Mycobacterium tuberculosis* Requires ESX-1-Mediated Secretion and Contributes to Pathogenesis. The Journal of Immunology *178*, 3143–3152. https://doi.org/10.4049/jimmunol.178.5.3143.
16. van der Wel, N., Hava, D., Houben, D., Fluitsma, D., van Zon, M., Pierson, J., Brenner, M., and Peters, P.J. (2007). M. tuberculosis and M. leprae Translocate from the Phagolysosome to the Cytosol in Myeloid Cells. Cell *129*, 1287–1298. https://doi.org/10.1016/j.cell.2007.05.059.
17. Coros, A., Callahan, B., Battaglioli, E., and Derbyshire, K.M. (2008). The specialized secretory apparatus ESX-1 is essential for DNA transfer in *Mycobacterium smegmatis*. Mol. Microbiol. *69*, 794–808. https://doi.org/10.1111/j.1365-2958.2008.06299.x.
18. Houben, D., Demangel, C., van Ingen, J., Perez, J., Baldeón, L., Abdallah, A.M., Caleechurn, L., Bottai, D., van Zon, M., de Punder, K., et al. (2012). ESX-1-mediated translocation to the cytosol controls virulence of mycobacteria. Cell. Microbiol. *14*, 1287–1298. https://doi.org/10.1111/j.1462-5822.2012.01799.x.
19. Abdallah, A.M., Gey van Pittius, N.C., DiGiuseppe Champion, P.A., Cox, J., Luirink, J., Vandenbroucke-Grauls, C.M.J.E., Appelmelk, B.J., and Bitter, W. (2007). Type VII secretion — mycobacteria show the way. Nat. Rev. Microbiol. *5*, 883–891. https://doi.org/10.1038/nrmicro1773.
20. Pym, A.S., Brodin, P., Majlessi, L., Brosch, R., Demangel, C., Williams, A., Griffiths, K.E., Marchal, G., Leclerc, C., and Cole, S.T. (2003). Recombinant BCG exporting ESAT-6 confers enhanced protection against tuberculosis. Nat. Med. *9*, 533–539. https://doi.org/10.1038/nm859.
21. Bitter, W., Houben, E.N.G., Bottai, D., Brodin, P., Brown, E.J., Cox, J.S., Derbyshire, K., Fortune, S.M., Gao, L.-Y., Liu, J., et al. (2009). Systematic Genetic Nomenclature for Type VII Secretion Systems. PLoS Pathog. *5*, e1000507. https://doi.org/10.1371/journal.ppat.1000507.
22. DiGiuseppe Champion, P.A., Champion, M.M., Manzanillo, P., and Cox, J.S. (2009). ESX-1 secreted virulence factors are recognized by multiple cytosolic AAA ATPases in pathogenic mycobacteria. Mol. Microbiol. *73*, 950–962. https://doi.org/10.1111/j.1365-2958.2009.06821.x.

23. van Winden, V.J.C., Damen, M.P.M., Ummels, R., Bitter, W., and Houben, E.N.G. (2019). Protease domain and transmembrane domain of the type VII secretion mycosin protease determine system-specific functioning in mycobacteria. Journal of Biological Chemistry *294*, 4806–4814. https://doi.org/10.1074/jbc.RA118.007090.
24. van Winden, V.J.C., Ummels, R., Piersma, S.R., Jiménez, C.R., Korotkov, K. V., Bitter, W., and Houben, E.N.G. (2016). Mycosins Are Required for the Stabilization of the ESX-1 and ESX-5 Type VII Secretion Membrane Complexes. mBio *7*. https://doi.org/10.1128/mBio.01471-16.
25. Costa, T.R.D., Felisberto-Rodrigues, C., Meir, A., Prevost, M.S., Redzej, A., Trokter, M., and Waksman, G. (2015). Secretion systems in Gram-negative bacteria: structural and mechanistic insights. Nat. Rev. Microbiol. *13*, 343–359. https://doi.org/10.1038/nrmicro3456.
26. McLaughlin, B., Chon, J.S., MacGurn, J.A., Carlsson, F., Cheng, T.L., Cox, J.S., and Brown, E.J. (2007). A Mycobacterium ESX-1–Secreted Virulence Factor with Unique Requirements for Export. PLoS Pathog. *3*, e105. https://doi.org/10.1371/journal.ppat.0030105.
27. Gao, L., Guo, S., McLaughlin, B., Morisaki, H., Engel, J.N., and Brown, E.J. (2004). A mycobacterial virulence gene cluster extending RD1 is required for cytolysis, bacterial spreading and ESAT-6 secretion. Mol. Microbiol. *53*, 1677–1693. https://doi.org/10.1111/j.1365-2958.2004.04261.x.
28. Stanley, S.A., Raghavan, S., Hwang, W.W., and Cox, J.S. (2003). Acute infection and macrophage subversion by Mycobacterium tuberculosis require a specialized secretion system. Proceedings of the National Academy of Sciences *100*, 13001–13006. https://doi.org/10.1073/pnas.2235593100.
29. Osman, M.M., Shanahan, J.K., Chu, F., Takaki, K.K., Pinckert, M.L., Pagán, A.J., Brosch, R., Conrad, W.H., and Ramakrishnan, L. (2022). The C terminus of the mycobacterium ESX-1 secretion system substrate ESAT-6 is required for phagosomal membrane damage and virulence. Proceedings of the National Academy of Sciences *119*. https://doi.org/10.1073/pnas.2122161119.
30. Xu, J., Laine, O., Masciocchi, M., Manoranjan, J., Smith, J., Du, S.J., Edwards, N., Zhu, X., Fenselau, C., and Gao, L. (2007). A unique *Mycobacterium* ESX-1 protein co-secretes with CFP-10/ESAT-6 and is necessary for inhibiting phagosome maturation. Mol. Microbiol. *66*, 787–800. https://doi.org/10.1111/j.1365-2958.2007.05959.x.
31. Huang, D., and Bao, L. (2016). Mycobacterium tuberculosis EspB protein suppresses interferon-γ-induced autophagy in murine macrophages. Journal of Microbiology, Immunology and Infection *49*, 859–865. https://doi.org/10.1016/j.jmii.2014.11.008.
32. Chen, J.M., Zhang, M., Rybniker, J., Boy-Röttger, S., Dhar, N., Pojer, F., and Cole, S.T. (2013). *Mycobacterium tuberculosis* EspB binds phospholipids and mediates EsxA-independent virulence. Mol. Microbiol. *89*, 1154–1166. https://doi.org/10.1111/mmi.12336.
33. Huang, D., and Bao, L. (2016). Mycobacterium tuberculosis EspB protein suppresses interferon-γ-induced autophagy in murine macrophages. Journal of Microbiology, Immunology and Infection *49*, 859–865. https://doi.org/10.1016/j.jmii.2014.11.008.
34. Ohol, Y.M., Goetz, D.H., Chan, K., Shiloh, M.U., Craik, C.S., and Cox, J.S. (2010). Mycobacterium tuberculosis MycP1 Protease Plays a Dual Role in Regulation of ESX-1 Secretion and Virulence. Cell

Host Microbe *7*, 210–220. https://doi.org/10.1016/j.chom.2010.02.006.

35. Piton, J., Pojer, F., Wakatsuki, S., Gati, C., and Cole, S.T. (2020). High resolution CryoEM structure of the ring-shaped virulence factor EspB from Mycobacterium tuberculosis. J. Struct. Biol. X *4*, 100029. https://doi.org/10.1016/j.yjsbx.2020.100029.
36. Solomonson, M., Huesgen, P.F., Wasney, G.A., Watanabe, N., Gruninger, R.J., Prehna, G., Overall, C.M., and Strynadka, N.C.J. (2013). Structure of the Mycosin-1 Protease from the Mycobacterial ESX-1 Protein Type VII Secretion System. Journal of Biological Chemistry *288*, 17782–17790. https://doi.org/10.1074/jbc.M113.462036.
37. Zhao, S., Jiang, X., Li, N., and Wang, T. (2024). SLMO transfers phosphatidylserine between the outer and inner mitochondrial membrane in Drosophila. PLoS Biol. *22*, e3002941. https://doi.org/10.1371/journal.pbio.3002941.
38. Baba, T., Kashiwagi, Y., Arimitsu, N., Kogure, T., Edo, A., Maruyama, T., Nakao, K., Nakanishi, H., Kinoshita, M., Frohman, M.A., et al. (2014). Phosphatidic Acid (PA)-preferring Phospholipase A1 Regulates Mitochondrial Dynamics. Journal of Biological Chemistry *289*, 11497–11511. https://doi.org/10.1074/jbc.M113.531921.
39. Chen, Y., Zhou, Z., and Min, W. (2018). Mitochondria, Oxidative Stress and Innate Immunity. Front. Physiol. *9*. https://doi.org/10.3389/fphys.2018.01487.
40. Bock, F.J., and Tait, S.W.G. (2020). Mitochondria as multifaceted regulators of cell death. Nat. Rev. Mol. Cell Biol. *21*, 85–100. https://doi.org/10.1038/s41580-019-0173-8.
41. Mehta, M.M., Weinberg, S.E., and Chandel, N.S. (2017). Mitochondrial control of immunity: beyond ATP. Nat. Rev. Immunol. *17*, 608–620. https://doi.org/10.1038/nri.2017.66.
42. Sengupta, N., Padmanaban, S., and Dutta, S. (2023). Cryo-EM reveals the membrane-binding phenomenon of EspB, a virulence factor of the mycobacterial type VII secretion system. Journal of Biological Chemistry *299*, 104589. https://doi.org/10.1016/j.jbc.2023.104589.
43. Gijsbers, A., Vinciauskaite, V., Siroy, A., Gao, Y., Tria, G., Mathew, A., Sánchez-Puig, N., López-Iglesias, C., Peters, P.J., and Ravelli, R.B.G. (2021). Priming mycobacterial ESX-secreted protein B to form a channel-like structure. Curr. Res. Struct. Biol. *3*, 153–164. https://doi.org/10.1016/j.crstbi.2021.06.001.
44. Söllner, T., Pfaller, R., Griffiths, G., Pfanner, N., and Neupert, W. (1990). A mitochondrial import receptor for the ADP/ATP carrier. Cell *62*, 107–115. https://doi.org/10.1016/0092-8674(90)90244-9.
45. Brix, J., Dietmeier, K., and Pfanner, N. (1997). Differential Recognition of Preproteins by the Purified Cytosolic Domains of the Mitochondrial Import Receptors Tom20, Tom22, and Tom70. Journal of Biological Chemistry *272*, 20730–20735. https://doi.org/10.1074/jbc.272.33.20730.
46. Korotkova, N., Piton, J., Wagner, J.M., Boy-Röttger, S., Japaridze, A., Evans, T.J., Cole, S.T., Pojer, F., and Korotkov, K. V. (2015). Structure of EspB, a secreted substrate of the ESX-1 secretion system of Mycobacterium tuberculosis. J. Struct. Biol. *191*, 236–244. https://doi.org/10.1016/j.jsb.2015.06.003.

47. Solomonson, M., Setiaputra, D., Makepeace, K.A.T., Lameignere, E., Petrotchenko, E.V., Conrady, D.G., Bergeron, J.R., Vuckovic, M., DiMaio, F., Borchers, C.H., et al. (2015). Structure of EspB from the ESX-1 Type VII Secretion System and Insights into its Export Mechanism. Structure *23*, 571–583. https://doi.org/10.1016/j.str.2015.01.002.
48. Crystal Structure of the Yeast Tom70 (2006). Preprint, https://doi.org/10.2210/pdb2gw1/pdb https://doi.org/10.2210/pdb2gw1/pdb.
49. Wu, Y., and Sha, B. (2006). Crystal structure of yeast mitochondrial outer membrane translocon member Tom70p. Nat. Struct. Mol. Biol. *13*, 589–593. https://doi.org/10.1038/nsmb1106.
50. Madeo, F., Carmona-Gutierrez, D., Ring, J., Büttner, S., Eisenberg, T., and Kroemer, G. (2009). Caspase-dependent and caspase-independent cell death pathways in yeast. Biochem. Biophys. Res. Commun. *382*, 227–231. https://doi.org/10.1016/j.bbrc.2009.02.117.
51. Kozjak-Pavlovic, V., Ross, K., and Rudel, T. (2008). Import of bacterial pathogenicity factors into mitochondria. Curr. Opin. Microbiol. *11*, 9–14. https://doi.org/10.1016/j.mib.2007.12.004.
52. Bouchez, C.L., Hammad, N., Cuvellier, S., Ransac, S., Rigoulet, M., and Devin, A. (2020). The Warburg Effect in Yeast: Repression of Mitochondrial Metabolism Is Not a Prerequisite to Promote Cell Proliferation. Front. Oncol. *10*. https://doi.org/10.3389/fonc.2020.01333.
53. Pathak, S.K., Basu, S., Basu, K.K., Banerjee, A., Pathak, S., Bhattacharyya, A., Kaisho, T., Kundu, M., and Basu, J. (2007). Direct extracellular interaction between the early secreted antigen ESAT-6 of Mycobacterium tuberculosis and TLR2 inhibits TLR signaling in macrophages. Nat. Immunol. *8*, 610–618. https://doi.org/10.1038/ni1468.
54. Pajuelo, D., Tak, U., Zhang, L., Danilchanka, O., Tischler, A.D., and Niederweis, M. (2021). Toxin secretion and trafficking by Mycobacterium tuberculosis. Nat. Commun. *12*, 6592. https://doi.org/10.1038/s41467-021-26925-1.
55. Osman, M.M., Shanahan, J.K., Chu, F., Takaki, K.K., Pinckert, M.L., Pagán, A.J., Brosch, R., Conrad, W.H., and Ramakrishnan, L. (2022). The C terminus of the mycobacterium ESX-1 secretion system substrate ESAT-6 is required for phagosomal membrane damage and virulence. Proceedings of the National Academy of Sciences *119*. https://doi.org/10.1073/pnas.2122161119.
56. Rivera-Calzada, A., Famelis, N., Llorca, O., and Geibel, S. (2021). Type VII secretion systems: structure, functions and transport models. Nat. Rev. Microbiol. *19*, 567–584. https://doi.org/10.1038/s41579-021-00560-5.
57. Conrad, W.H., Osman, M.M., Shanahan, J.K., Chu, F., Takaki, K.K., Cameron, J., Hopkinson-Woolley, D., Brosch, R., and Ramakrishnan, L. (2017). Mycobacterial ESX-1 secretion system mediates host cell lysis through bacterium contact-dependent gross membrane disruptions. Proceedings of the National Academy of Sciences *114*, 1371–1376. https://doi.org/10.1073/pnas.1620133114.
58. Wilke, G.A., and Wardenburg, J.B. (2010). Role of a disintegrin and metalloprotease 10 in *Staphylococcus aureus* α-hemolysin–mediated cellular injury. Proceedings of the National Academy of Sciences *107*, 13473–13478. https://doi.org/10.1073/pnas.1001815107.

59. Kwok, T., Zabler, D., Urman, S., Rohde, M., Hartig, R., Wessler, S., Misselwitz, R., Berger, J., Sewald, N., König, W., et al. (2007). Helicobacter exploits integrin for type IV secretion and kinase activation. Nature *449*, 862–866. https://doi.org/10.1038/nature06187.

60. Jain, P., Luo, Z.-Q., and Blanke, S.R. (2011). *Helicobacter pylori* vacuolating cytotoxin A (VacA) engages the mitochondrial fission machinery to induce host cell death. Proceedings of the National Academy of Sciences *108*, 16032–16037. https://doi.org/10.1073/pnas.1105175108.

61. Galmiche, A., Rassow, J., Doye, A., Cagnol, S., Chambard, J., Contamin, S., de Thillot, V., Just, I., Ricci, V., Solcia, E., et al. (2000). The N-terminal 34 kDa fragment of Helicobacter pylori vacuolating cytotoxin targets mitochondria and induces cytochrome c release. EMBO J. *19*, 6361–6370. https://doi.org/10.1093/emboj/19.23.6361.

62. Merritt, E.A., Sarfaty, S., Akker, F. Van Den, L'Hoir, C., Martial, J.A., and Hol, W.G.J. (1994). Crystal structure of cholera toxin B-pentamer bound to receptor G_{M1} pentasaccharide. Protein Science *3*, 166–175. https://doi.org/10.1002/pro.5560030202.

63. Nerlich, A., Mieth, M., Letsiou, E., Fatykhova, D., Zscheppang, K., Imai-Matsushima, A., Meyer, T.F., Paasch, L., Mitchell, T.J., Tönnies, M., et al. (2018). Pneumolysin induced mitochondrial dysfunction leads to release of mitochondrial DNA. Sci. Rep. *8*, 182. https://doi.org/10.1038/s41598-017-18468-7.

64. Braun, J.S., Hoffmann, O., Schickhaus, M., Freyer, D., Dagand, E., Bermpohl, D., Mitchell, T.J., Bechmann, I., and Weber, J.R. (2007). Pneumolysin Causes Neuronal Cell Death through Mitochondrial Damage. Infect. Immun. *75*, 4245–4254. https://doi.org/10.1128/IAI.00031-07.

65. Lacy, D.B., Wigelsworth, D.J., Melnyk, R.A., Harrison, S.C., and Collier, R.J. (2004). Structure of heptameric protective antigen bound to an anthrax toxin receptor: A role for receptor in pH-dependent pore formation. Proceedings of the National Academy of Sciences *101*, 13147–13151. https://doi.org/10.1073/pnas.0405405101.

66. Nguyen, A.H., Thomsen, A.R.B., Cahill, T.J., Huang, R., Huang, L.-Y., Marcink, T., Clarke, O.B., Heissel, S., Masoudi, A., Ben-Hail, D., et al. (2019). Structure of an endosomal signaling GPCR–G protein–β-arrestin megacomplex. Nat. Struct. Mol. Biol. *26*, 1123–1131. https://doi.org/10.1038/s41594-019-0330-y.

67. MacGurn, J.A., and Cox, J.S. (2007). A Genetic Screen for *Mycobacterium tuberculosis* Mutants Defective for Phagosome Maturation Arrest Identifies Components of the ESX-1 Secretion System. Infect. Immun. *75*, 2668–2678. https://doi.org/10.1128/IAI.01872-06.

68. Tan, T., Lee, W.L., Alexander, D.C., Grinstein, S., and Liu, J. (2006). The ESAT-6/CFP-10 secretion system of Mycobacterium marinum modulates phagosome maturation. Cell. Microbiol. *8*, 1417–1429. https://doi.org/10.1111/j.1462-5822.2006.00721.x.

69. Simeone, R., Bobard, A., Lippmann, J., Bitter, W., Majlessi, L., Brosch, R., and Enninga, J. (2012). Phagosomal Rupture by Mycobacterium tuberculosis Results in Toxicity and Host Cell Death. PLoS Pathog. *8*, e1002507. https://doi.org/10.1371/journal.ppat.1002507.

70. Stanley, S.A., Raghavan, S., Hwang, W.W., and Cox, J.S. (2003). Acute infection and macrophage subversion by Mycobacterium tuberculosis require a specialized secretion system. Proceedings of the National Academy of Sciences *100*, 13001–13006. https://doi.org/10.1073/pnas.2235593100.
71. Guinn, K.M., Hickey, M.J., Mathur, S.K., Zakel, K.L., Grotzke, J.E., Lewinsohn, D.M., Smith, S., and Sherman, D.R. (2004). Individual RD1-region genes are required for export of ESAT-6/CFP-10 and for virulence of *Mycobacterium tuberculosis*. Mol. Microbiol. *51*, 359–370. https://doi.org/10.1046/j.1365-2958.2003.03844.x.
72. Huang, D., and Bao, L. (2016). Mycobacterium tuberculosis EspB protein suppresses interferon-γ-induced autophagy in murine macrophages. Journal of Microbiology, Immunology and Infection *49*, 859–865. https://doi.org/10.1016/j.jmii.2014.11.008.
73. Introducing Monolith X with breakthrough Spectral Shift Technology https://nanotempertech.com/monolith/.
74. Mo.Affinity analysis software https://shop.nanotempertech.com/mo-affinity-analysis-software-unlimited-licenses/.
75. Tang, G., Peng, L., Baldwin, P.R., Mann, D.S., Jiang, W., Rees, I., and Ludtke, S.J. (2007). EMAN2: An extensible image processing suite for electron microscopy. J. Struct. Biol. *157*, 38–46. https://doi.org/10.1016/j.jsb.2006.05.009.
76. Swift, M. L. Graphpad prism, data analysis, and scientific graphing (1997). Chem. Inf. Comput. Sci *37*, 411–412.
77. Kumar, A., P., S., Gulati, S., and Dutta, S. (2021). User-friendly, High-throughput, and Fully Automated Data Acquisition Software for Single-particle Cryo-electron Microscopy. Journal of Visualized Experiments. https://doi.org/10.3791/62832.
78. Goddard, T.D., Huang, C.C., Meng, E.C., Pettersen, E.F., Couch, G.S., Morris, J.H., and Ferrin, T.E. (2018). UCSF ChimeraX: Meeting modern challenges in visualization and analysis. Protein Science *27*, 14–25. https://doi.org/10.1002/pro.3235.
79. Scheres, S.H.W., and Chen, S. (2012). Prevention of overfitting in cryo-EM structure determination. Nat. Methods *9*, 853–854. https://doi.org/10.1038/nmeth.2115.
80. Piton, J., Pojer, F., Wakatsuki, S., Gati, C., and Cole, S.T. (2020). CryoEM structure of the ring-shaped virulence factor EspB from Mycobacterium tuberculosis. Preprint, https://doi.org/10.2210/pdb6xzc/pdb https://doi.org/10.2210/pdb6xzc/pdb.
81. Emsley, P., and Cowtan, K. (2004). *Coot*: model-building tools for molecular graphics. Acta Crystallogr. D Biol. Crystallogr. *60*, 2126–2132. https://doi.org/10.1107/S0907444904019158.
82. Daniel Gietz, R., and Woods, R.A. (2002). Transformation of yeast by lithium acetate/single-stranded carrier DNA/polyethylene glycol method. In, pp. 87–96. https://doi.org/10.1016/S0076-6879(02)50957-5.
83. Bankapalli, K., Vishwanathan, V., Susarla, G., Sunayana, N., Saladi, S., Peethambaram, D., and D'Silva, P. (2020). Redox-dependent regulation of mitochondrial dynamics by DJ-1 paralogs in Saccharomyces cerevisiae. Redox Biol. *32*, 101451. https://doi.org/10.1016/j.redox.2020.101451.

84. Schindelin, J., Arganda-Carreras, I., Frise, E., Kaynig, V., Longair, M., Pietzsch, T., Preibisch, S., Rueden, C., Saalfeld, S., Schmid, B., et al. (2012). Fiji: an open-source platform for biological-image analysis. Nat. Methods *9*, 676–682. https://doi.org/10.1038/nmeth.2019.

Figures

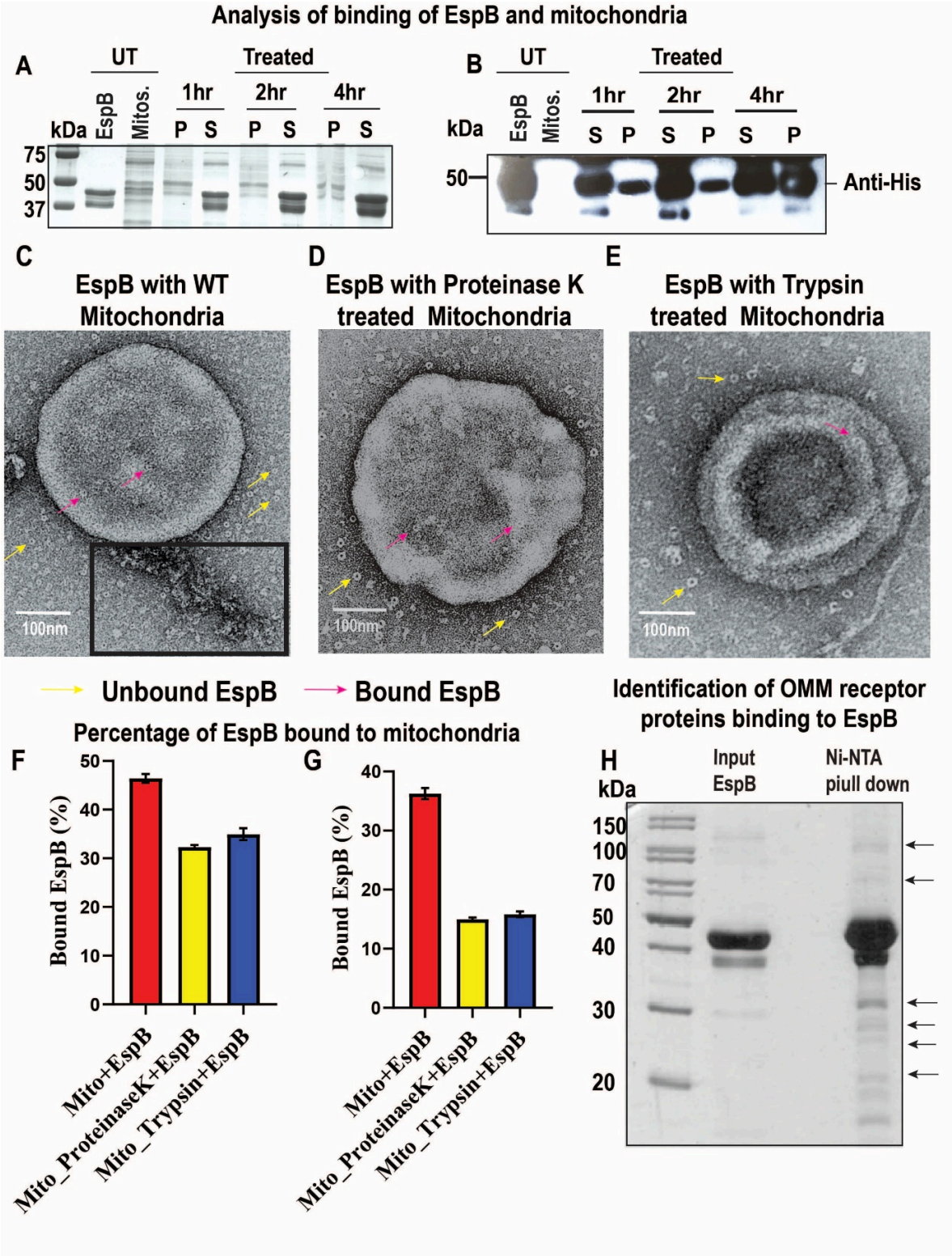


Figure 1

$EspB_{1-332}$ interaction with Mitochondria:

A. Mitochondrial sedimentation assay to assess the binding of EspB to mitochondria (12% SDS-PAGE), carried out at different time intervals. Supernatant (**S**) and pellet (**P**), EspB-treated (**Treated**) and untreated (**UT**). **B.** Western blot of the membrane corresponding to the mitochondrial sedimentation assay shown in Figure **1A**. EspB was detected using an anti-His antibody. **C.** NS-TEM micrograph of EspB incubated with isolated mitochondria. **D, E.** Representative NS-TEM micrographs of EspB and enzymatically pretreated mitochondria with Proteinase K and Trypsin, respectively. TEM images indicated that, after Proteinase K and Trypsin treatment, most of the EspB oligomers were observed on the background, and a very few EspB oligomers on mitochondria, which was different from the control samples (EspB with untreated mitochondria, where the majority of EspB oligomers were bound to the mitochondria) shown in **Figure 1C**. **F, G.** Bar diagrams showing the number of particles bound per mitochondrion, as analysed from the NS-TEM and cryo-EM datasets, respectively, indicating that EspB has a lower affinity for Proteinase K and Trypsin-treated mitochondria. **H.** Pull-down assay (immunoprecipitation) of EspB and mitochondria was performed and analysed by SDS-PAGE to identify the mitochondrial outer membrane EspB-associated proteins. SDS-PAGE gels showed clear EspB bands in both the control and the experimental (Ni-NTA pull-down) samples, but the Ni-NTA pull-down sample showed multiple additional bands, in addition to the strong EspB band, indicating that EspB likely interacts with one or more mitochondrial membrane proteins.

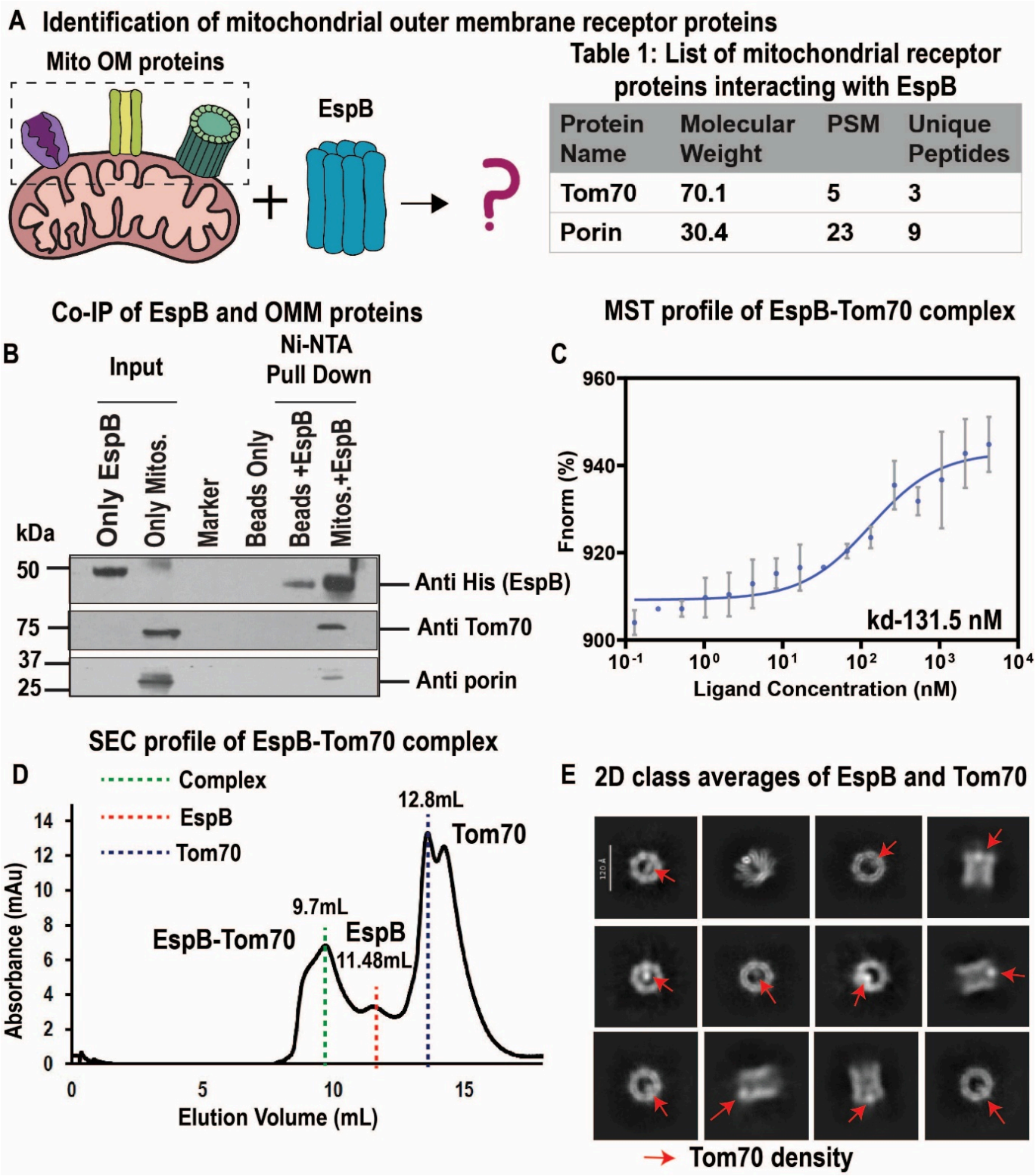


Figure 2

Characterisation of the $EspB_{1-332}$ -Tom70 interaction.

A. Schematic representation of the outer mitochondrial membrane proteins that bind to EspB. Mass spectrometry analysis of the Ni-NTA pull-down bands (**Figure 1H**) strongly suggested that Tom70 and porin were present in the Ni-NTA SDS-PAGE gel. The table shows a few mitochondrial membrane

proteins that might be responsible for EspB binding. Outer mitochondrial membrane proteins were selected based on their higher PSM values and known functions. **B.** Immunoblot corresponding to the co-immunoprecipitation assay, probed with anti-Tom70 and anti-porin antibodies, showed an intense Tom70 band at ~70 kDa and a faint porin band at ~30 kDa, which clearly indicates that Tom70 and porin are the two proteins that associate with EspB during the pull-down assay. **C.** Microscale thermophoresis (MST) showed the binding affinity between EspB and Tom70. The overall dissociation constant (K_d) was approximately 131.5 nM, which is quite high for a protein–protein interaction. Data represent the mean ± SD of two independent runs from two independent purifications. **D.** Size-exclusion chromatography (SEC) profile of EspB and Tom70 revealed three distinct peaks, which are marked separately. The EspB–Tom70 complex is marked in green, EspB in red, and Tom70 in blue. **E.** Reference-free 2D classification of the EspB-Tom70 complex, where circular ring-like top views and two parallel side views are visible. In top-view 2D averages, a small additional density is observed at the centre of the circular ring-like structure. On the other hand, small dot-like densities are visible in the side views, which clearly indicate that the extra densities attached to the bottom of EspB might correspond to Tom70, as these densities are absent in EspB alone (2D averages of EspB are shown in **Supplementary Figure S4**). The Tom70 density is marked in red.

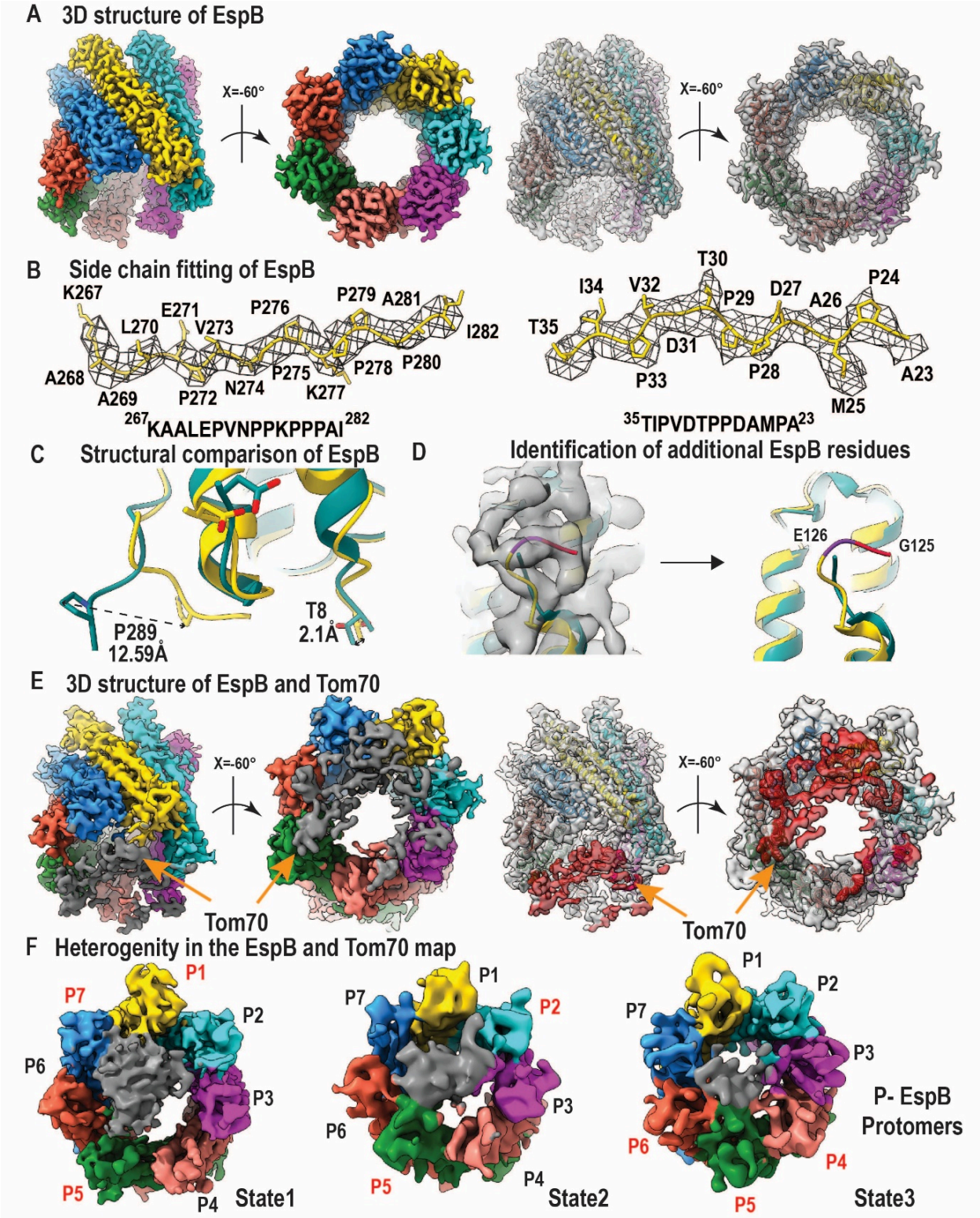
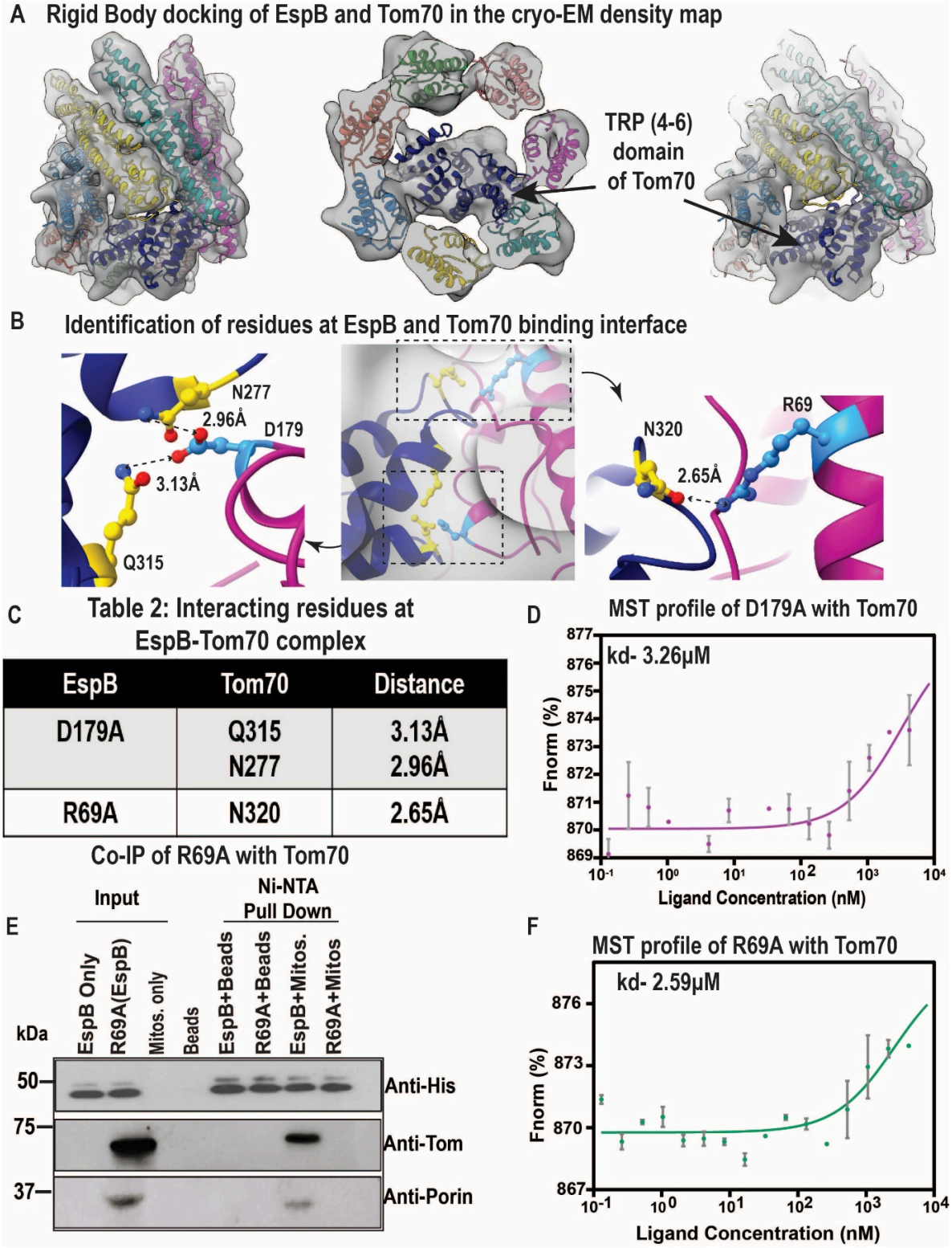


Figure 3

Structural characterisation of the EspB and EspB–Tom70 complexes.

A. 3D reconstruction of the EspB heptamer. The lateral and top views of EspB are shown, with an overall global resolution of 3.2 Å. The individual protomers are colored differently to highlight the heptameric assembly. The cryo-EM map is fitted with the corresponding atomic model (cartoon), which was built

from it. Structures are displayed at 0° and -60 ° orientations. Overall agreement between the map and model is very good. **B.** The side-chain fitting of the EspB atomic model (residues K267–I282 and A23–T35) into the cryo-EM density map shows excellent agreement between the amino acid side chains and the density, highlighting the high-resolution quality of the reconstruction. **C.** Structural superimposition of the EspB model generated in this study (**PDB-26UN**) with the previously reported structure (**PDB-6XZC**) is shown to identify conformational differences between the two structures. Only a few minor deviations were observed between the two structures, and the major deviation was observed at residue P289. P289 belongs to the flexible C-terminal region (P^{279}–P^{332}) of EspB, and a major deviation in this region is expected. The residues with the largest conformational changes are shown in ball-and-stick representation. **D.** The extra density obtained from the cryo-EM map of EspB allowed modelling of atomic coordinates of two additional residues, which were unresolved in the previously reported structure (**PDB-6XZC**). **E.** 3D reconstruction of the EspB–Tom70 complex resolved at a global resolution of 5.08 Å. Top and lateral views are shown, with individual EspB protomers colored differently to highlight the heptameric assembly. An additional density corresponding to Tom70 was observed in the proximal region of the map, near the C-terminus of the EspB protomers. The EspB atomic model was fitted into the cryo-EM density map of the EspB-Tom70 complex. The additional Tom70 density is highlighted in red. **F.** Heterogeneous refinement of the EspB-Tom70 complex revealed different binding positions of Tom70 across distinct EspB protomers, indicating a dynamic receptor arrangement. P represents the different protomers of EspB. The red labels indicate the EspB protomers directly associated with Tom70. Tom70 can bind to different combinations of protomers, such as P1, P5, and P7; P2 and P5; or P4, P5, and P6.



EspB	Tom70	Distance
D179A	Q315 N277	3.13Å 2.96Å
R69A	N320	2.65Å

Figure 4

Structural analysis and mutational validation of the EspB-Tom70 interaction.

A. Rigid-body docking of EspB (**PDB: 26UN**) and Tom70 (**PDB: 2GW1**) into the State 3 of EspB-Tom70 complex cryo-EM map. The cross-sectional and tilted views are shown, with Tom70 coloured in blue and individual EspB protomers coloured separately. Overall, the fitting is reasonable. **B.** From this rigid-body

docking, the interaction interface between Tom70 and EspB was identified. Residues present at the interacting surface are identified, and their distances are shown. **C.** Table showing the interacting residues of the EspB–Tom70 complex. **D, F.** Microscale thermophoresis (MST) assays of EspB mutants (D179A and R69A) with Tom70 were performed to measure their binding affinity. The MST profile indicated that the mutants have weaker binding affinities (K_d = 3.26 μM and 2.59 μM, respectively) than the wild type. Data represent the mean ± SD of two independent runs from two independent purifications. **E.** Immunoblot showing the co-immunoprecipitation of wild-type EspB and the R69A mutant with Tom70. The immunoblot demonstrates the presence of Tom70 and porin proteins.

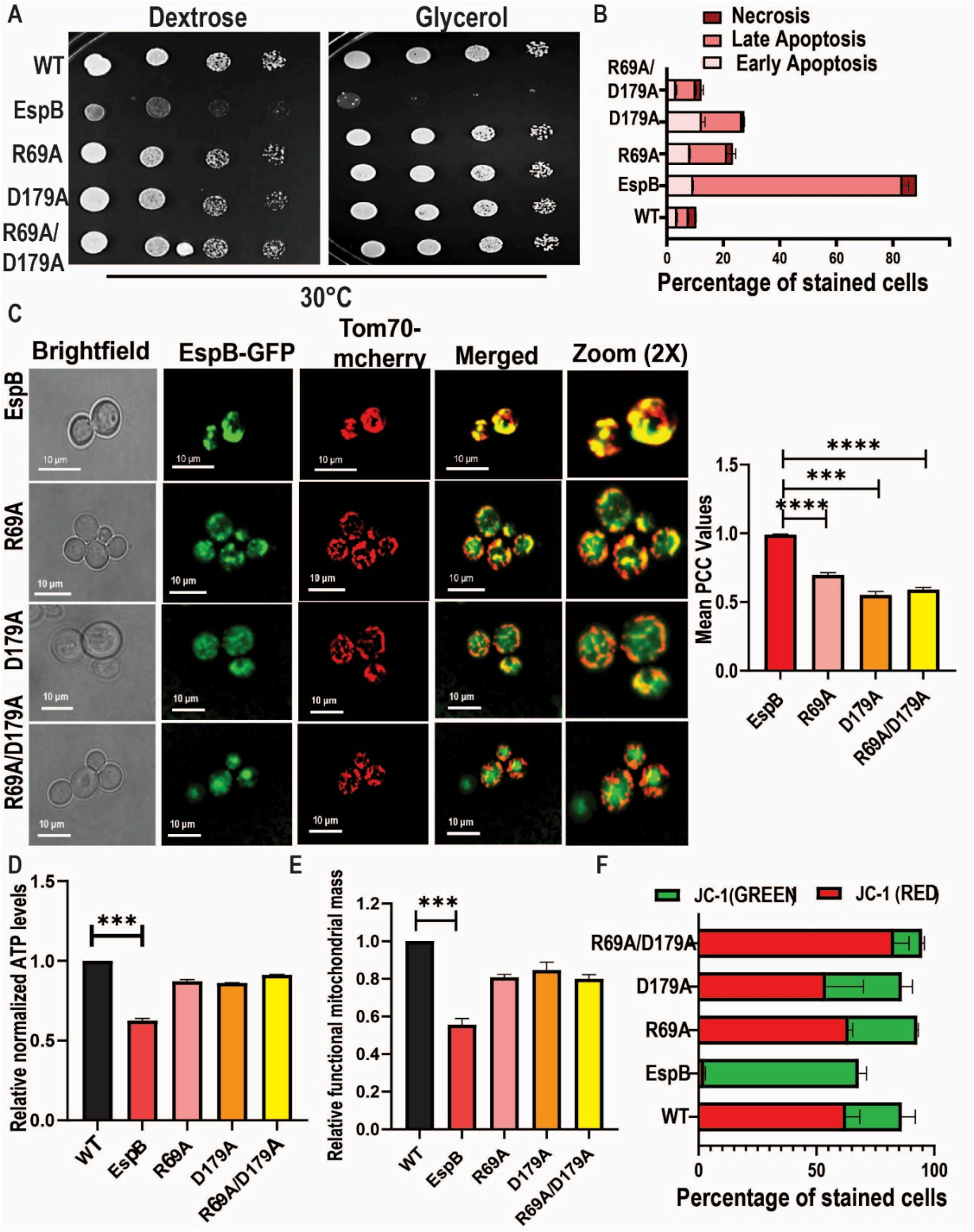


Figure 5

EspB induced mitochondrial dysfunction and compromised yeast cell viability.

A. $EspB_{1-322}$ and its mutants were expressed under high-expression promoters and cultured in dextrose medium at 30°C. Cells from mid-log phase were harvested, spotted onto both fermentative (dextrose) and respiratory (glycerol) media, and incubated at the permissive temperature. EspB-expressing cells

showed a severe growth phenotype in both dextrose and glycerol media compared to their mutants. Images of the plates were captured within a 36-48h window. **B**. The bar graph shown here, based on the apoptotic profiles in Supplementary Figure **S9C**, depicts the percentage of cells in the apoptotic profiles for the indicated strains when cultured in glycerol media. EspB shows a higher population of cells in apoptotic stages than its mutant strains. **C**. Colocalisation studies of $EspB_{1-332}$ and its mutant variants. $EspB_{1-332}$ and its mutations in the interactive residues (R69A, D179A and corresponding double mutant R69A/D179A) containing the GFP tag were transformed into yeast cells harbouring the Tom70-mCherry construct. Cells were grown in Ura-His glycerol medium and spread on a 2% agarose pad to visualise them under the Olympus Floview 3000 confocal microscope. EspB-GFP, merged with the mitochondrial protein Tom70-mCherry, shows clear overlap in protein localisation. Images were processed using Cell Sens software, followed by Image J software to analyse Pearson's coefficient for colocalisation. **D, E.** Flow cytometry was used to quantify the total mitochondrial potential in the $EspB_{1-332}$ and mutant strains, and the results were represented as bar graphs. The strains were stained with the potentiometric dyes TMRE and JC-1, followed by analysis on a CytoFLEX flow cytometer. The data were analysed using CytExpert software, which indicated the greatest loss of mitochondrial potential in EspB-containing cells compared to their mutants. **F**. Total mitochondrial ATP production from the above-mentioned strains was measured using the Mitochondrial ToxGlo Assay kit (Promega). Fluorescence reading was taken with excitation and emission at ~485/520 nm. Overall damage to mitochondrial potential caused by EspB overexpression results in a loss of mitochondrial ATP production, as indicated by the bar diagrams. However, its mutants did not affect mitochondrial energy flux.

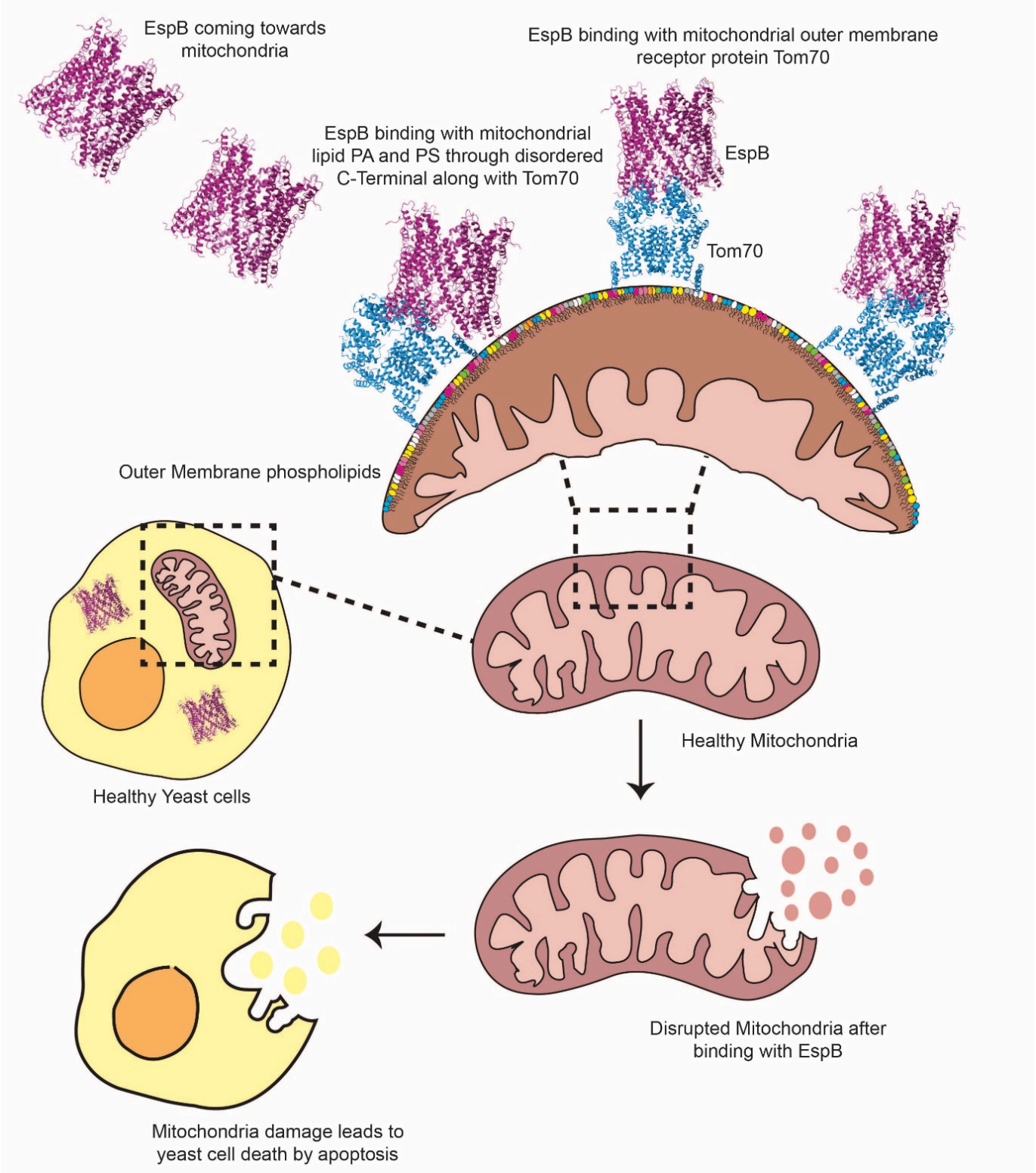


Figure 6

Proposed mechanism of EspB binding to mitochondria and killing the host cell.

Schematic diagram showing EspB binding to mitochondrial outer membrane receptor protein Tom70 and lipid, thereby damaging the host mitochondria and ultimately leading to host cell apoptosis. The PA molecules are marked in green, the PS molecules in white, Tom70 in blue, and EspB in purple.

Supplementary Files

This is a list of supplementary files associated with this preprint. Click to download.

- WesternBlots.pdf
- Supplementarytables.docx
- Supplementaryfigurefile.docx